Natural Land subsidence in Britain: A comparative review utilising downstream InSAR data products from the EGMS and SubCoast potential subsidence map

Submitted 25th August 2023, in partial fulfillment of
the conditions for the award of the degree **MRes Geospatial Data Science.**

David Fountain
20489590

Supervised by Professor Stuart Marsh (UoN), Luke Bateson (BGS)

Nottingham Geospatial Institute
University of Nottingham

I hereby declare that this dissertation is all my own work, except as indicated in the text.

Abstract

Land subsidence presents a global problem to many communities around the world, and the effects are predicted to get more substantial in the coming years due to the ensuing impacts of climate change. Although most observed land subsidence is as a result of human activities, geological deposits naturally undergo forms of subsidence without this impetus and measurements of the potential natural subsidence rates are important for planning purposes, risk management, and hazard mapping. Over the last few years there has been an increase in the availability of wide-are mapping of ground motion velocities from initiatives such as the European Ground Motion Service (EGMS). This has been made possible by the combined advances in Synthetic Aperture Radar satellite technology, sophisticated Interferometric Synthetic Aperture Radar (InSAR) processing algorithms, and the development of powerful cloud computing technologies that are capable of processing huge amounts of data.

The purpose of this dissertation project is to estimate the potential rates of natural subsidence stemming from dissolution, compaction, and shrinkage throughout Britain, by integrating InSAR velocities from the EGMS and derived maximum potential subsidence rates from the British Geological Survey project SubCoast. Several ancillary datasets were included to contextualise regions of motion to understand the underlying mechanisms, and correlations were analysed between average InSAR velocities and geological deposits to link the ground motion to natural processes.

The national-level analysis showed that the dominant trend of land subsidence in Britain is as a result of large-scale crustal movements, which are inline with Post-Glacial Isostatic Adjustments (GIA) as measured by continuous GNSS stations. Local scale analysis of the Greater London area determined the principle sources of motion as a result of groundwater abstraction and underground construction work, with other significant motions due to compaction of alluvium deposits surrounding the Thames estuary. At both a national and local level, the underlying geology had a minimal correlation with the observed motions. This highlights the possibilities of conducting ground deformation analysis at scale, through the use of large downstream data products.

Acknowledgements

A big thanks to my supervisors Stuart Marsh and Luke Bateson for their time, suggestions, and expertise, as well as additional input from Alessandro Novellino and Lee Jones from BGS, and to BGS in general for supplying the SubCoast and superficial thickness data and for sponsoring the project. Finally, thanks to the Engineering and Physical Sciences Research Council (EPSRC) for providing the funding through the Geospatial Systems CDT programme.

Contents

List of Tables

List of Figures

0.1 Introduction

Land subsidence (LS) is a global phenomenon that may be defined as the vertical downward displacement of the Earth's surface, which develops from a broad range of sub-surface processes arising from both natural causes and anthropogenic activities [45]. The type of ground motion that is observed in a particular area is controlled by the physical characteristics of the surrounding soils and rocks; carbonate rocks such as limestone are susceptible to dissolution by groundwater, which can create underground cave networks that lead to sudden collapsing deposits and sinkholes [57], whereas clay-rich soils have high potential to undergo swelling and shrinking in response to increasing and decreasing levels of water content [41]. The occurrence of natural subsidence can include the gradual regional-level lowering of the ground surface as well as sudden, localised sinking events, brought about by the cyclical geological processes of earth movement, denudation, and deposition [55]. Although naturally occurring subsidence is prevalent worldwide, human activities can directly enhance these effects and are often the root cause. The most common source of human-induced LS is the exploitation of groundwater, which contributes to over 80% of the identified subsidence in the US [10]. The principle uses of this include irrigation of agricultural land and the production of drinking water, which can lead to local and regional groundwater storage depletion and compaction of susceptible aquifer systems, resulting in LS related to the groundwater-level decline [37].

The consequences of LS are widespread, including environmental impacts in the form of the decline in ground elevation and an increase in flooding potential, and economic impacts resulting from damage to surface and underground infrastructure and cracking and collapsing of civil structures [21]. In Britain, the economic cost of LS is estimated to be £3 billion over the last decade [26], which is set to increase in future, with predictions by the British Geological Survey (BGS) indicating that the number of properties in Britain facing issues and damage from shrink-swell will likely reach 10% by 2070, up from 3% in 1990, due to climate-related factors [26]. Of particular concern are coastal delta cities, where land subsidence and sea level rise (SLR) contribute to increased relative SLR (RSLR) and an enhanced susceptibility to flood risk, with parts of major cities projected to sink below sea level in the future [33]. For these reasons, it is important that the underlying mechanisms of LS are understood and any potential hazards are identified in advance.

0.2 Motivation

The principal motivation for this project is to utilise downstream Big-InSAR data products to map natural subsidence rates stemming from the processes of compaction, dissolution, and shrinkage, on a national-scale over Britain. With LS predicted to effect more households over the next 50 years due to climate change, understanding which areas and communities are most at risk of LS is key for effective planning of buildings and infrastructure, and for mitigating the future economic costs and health impacts of subsidence based damage. The project is facilitated by the integration of two key datasets; Interferometric Synthetic Aperture Radar (InSAR) ground displacement velocities from the European Ground Motion Service (EGMS), and SubCoast natural

Potential Subsidence Rates (PSR) from BGS. A secondary motivation for this project is to develop a case study for the use of EGMS data for national-scale geohazard mapping, which can be developed upon in future work as part of the PhD.

As this MRes project is delivered and funded through the EPSRC Geospatial Systems CDT programme, it has been established to correspond with the specific CDT themes. The project primarily aligns with the *Translation to Global Challenges* and *Urban and Infrastructure Resilience* themes, as LS is a global problem which affects communities and civil structures in various geographic locations, often in urban coastal and river delta areas.

0.3 Aims and Objectives

In accordance with the motivations behind this project, the main objectives include:

1. A comparison and analysis of PSR and EGMS velocities throughout Britain and the correlation with the underlying geology.
2. A case study into the subsidence around the Thames estuary.
3. Re-calibration of natural PSR for Britain.

The aim of meeting these specific objectives would be to create a more accurate, natural subsidence map of Britain that could be utilised for hazard mapping, or as a feature input to a more comprehensive model for determining sources of ground motion.

0.4 Dissertation Structure

The remaining sections of the dissertation detail the steps in integrating and comparing the SubCoast and EGMS datasets and the derivation of updated natural subsidence rates for Britain, the methodologies used to achieve this, and the background work and concepts that this research builds upon. These sections are as follows:

1. **Background and Related Work**
   This chapter focuses on the context of the dissertation, and provides background concepts on techniques and terminology used during the project.
2. **Methodology**
   This chapter introduces the input datasets and an overview of how they are combined, and outlines the analysis methods and the software programmes used to conduct this project.
3. **Results**
   This chapter lists the results obtained during the analysis. These are presented in the form of tables, graphs, and maps, for the national-level and local London area.
4. **Discussion**
   This chapter discusses some of the outputs of the results section in further detail and ties together some results from the wider literature to contextualise the findings.
5. **Evaluation and Conclusion**

The final section discusses the overall success of the project, and critically evaluates the outputs obtained in the results section and suggests areas of improvement and additional work.

Chapter 1

Background and Related Work

This chapter presents some of the background concepts and techniques used in this MRes project, including an overview of the land subsidence considered in this project, and common methods and data that are available to track these effects. As the project only utilises the downstream outputs of D-InSAR processing, rather than computing this from raw SAR data, only a short, basic overview of SAR and InSAR are presented here.

1.1 Land Subsidence

The effects of LS are extensive and include a variety of physical characteristics which are present over different spatial and temporal scales. For instance, slow long-term movements in the ground surface which are present over large areas can be observed from phenomena such as sediment de-watering or mining activity, whereas instantaneous ground collapse, such as from sinkholes, cause significant disruption to small localised areas but are separated by long periods of stability [53]. These effects are also typical of the basis of ground motion; the effects of LS from purely natural processes such as tectonic movement, rock solution, and deep sediment compaction, are primarily very slow and have a limited impact on engineering time scales, while anthropogenic activity can induce more rapid and serious subsidence [53]. The remaining parts of this section introduce some of the different types of LS and the underlying geological processes that lie behind the subsidence mechanisms.

1.1.1 Dissolution

Dissolution is the process by which soluble rocks such as limestone, chalk, dolomite, gypsum, and halite are dissolved by the passage of water, or weakly acidic water, over the rock surfaces or through fractures and pores in the rock [31]. Water in the atmosphere can dissolve small amounts of carbon dioxide (CO_2) which leads to a small amount of carbonic acid (H_2CO_3) in the rain water that falls to the ground. The calcite in carbonate rocks (e.g. limestone, chalk) reacts with the carbonic acid, which produces dissolved calcium and bicarbonate ions, and leads to the formation of cavities over time [57].

Through the described processes of chemical dissolution, underground caves can form as a result of groundwater flow. When these subsurface cave structures collapse, sink-

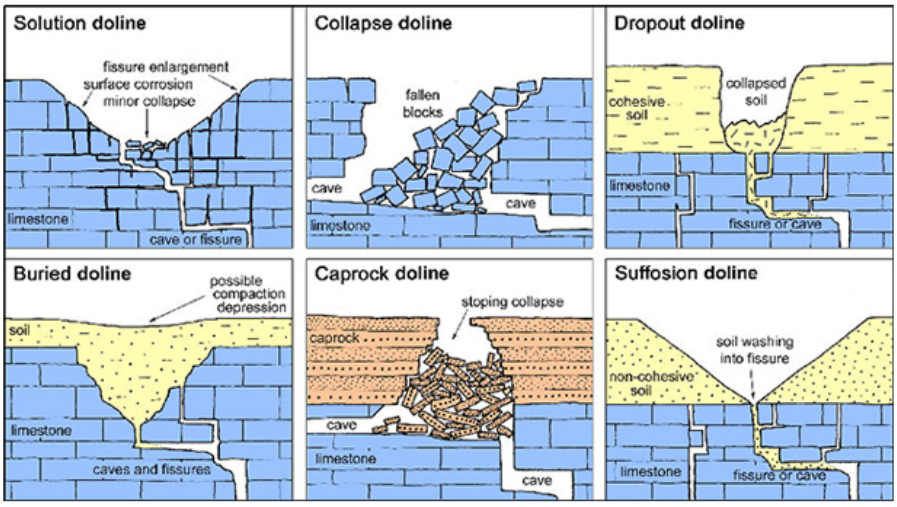

Figure 1.1: Classification of sinkhole types. Source: [16].

holes are formed on the surface where the top layer of materials fall in to the exposed caves. Typically, these sinkholes are formed as a result of the lowering of the water table which removes support for the underlying cavern ceiling [57]. Other types of sinkhole are created from sediment downwashing into rock fissures, which doesn't involve any failure of the underlying bedrock (see Figure 1.1 for examples of types of sinkholes). The depth of subsidence and width of sinkhole are related to the soil thickness, soil slope stability, and the physical characteristics of the soil deposits; the subsiding area width may be five times the depth in loose sands, whilst three times the depth in boulder clay [53]. Furthermore, although subsidence sinkholes are normally less frequent in areas with thicker soil depths, variations in permeability and drainage make identifying wide-scale limits problematic, and sinkholes which pose significant risk have been found in soil depths between 5 to 50 m in different parts of the world [53]. Due to these reasons, predicting the occurrence of sinkholes is a challenging task.

1.1.2 Compaction

The compaction of soil relates to the physical process of reducing the voids of a sediment as a result of its mineral grains being squeezed together when under an external load [41]. Certain types of ground contain layers of very soft materials like clay or peat, which can compress if loaded by overlying structures or if the groundwater level changes [3]. In the process of consolidation, the ground compresses as the applied load causes fluid in the pore space between its solid components to squeeze out, resulting in a rapid decrease in thickness. The distinction between consolidation and compaction is that compaction is a mechanical, immediate process, which only occurs in soils with a proportion of sand [39], although these effects often seem to be reported together. The amount of subsidence rising from these processes is a function of the pore space in the original material, the effectiveness of the compacting mechanism, and the thickness of the deposit undergoing compaction [39]. Typical deposits which undergo varying gradations of compressibility include peat, alluvium and laminated clays [3].

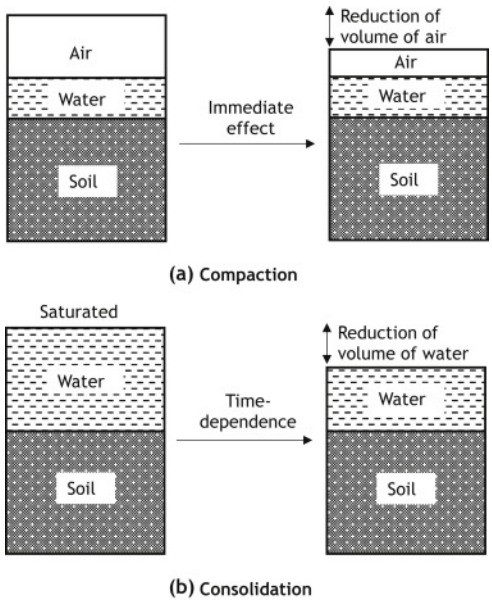

Figure 1.2: Example of compaction and consolidation. Source: Dhir et al - Use of Copper Slag in Geotechnical Applications [32]

Hydrocompaction

Hydrocompaction effects loose, dry sedimentary materials, which are prone to collapse when water is added to them. The effected materials are mainly very-fine textured sediments such as sand and silt, which have remained in arid conditions; the strength of these sediments is derived from the intergranular bonds between grains (usually containing a small amount of clay) which fail when water is added, leading to soil collapse [53]. The magnitude and area of the resulting subsidence is controlled by the thickness of the collapsing soil and the stress on the soil from overlying loads, which can induce subsidence to a depth of 5 m over wide areas [53].

1.1.3 Shrink Swell

Shrink-swell relates to the periodic wetting and drying of clay-rich soils, which leads to the sediment absorbing liquid and expanding during the wetting process (causing uplift, or heave, of the ground surface), and shrinking as the soil drys out (causing subsidence). The mechanisms of shrinkage differ from that of compaction and consolidation, where the amount of subsidence is a function of the soil void and thickness, and overlying structural load, whereas shrinkage is a process involving soil physics [39]. The water content of a clay plays a significant role in its behaviour; when the clay is saturated with water it behaves like a viscous liquid, and gradually thickens before becoming hard and solid as the water content reduces. These phases of behaviour are characterised by the liquid, plastic, and shrinkage limits of the clay, which denote the boundaries of the water content where the different qualities are present [41]. The range between the liquid and plastic limits, known as the plasticity index, alongside the proportion of clay particles finer than 2 μm, define the shrinking and swelling potential of the clay. Finer clay deposits with a high plasticity index have a higher swelling potential, and thus a higher shrinkage potential (see Figure 1.3).

In addition to clay-rich soils, superficial deposits such as alluvium and peat are also susceptible to soil subsidence and uplift [22]. As this project is concerned with subsi-

dence, we are mainly interested in the shrinkage qualities of the soil.

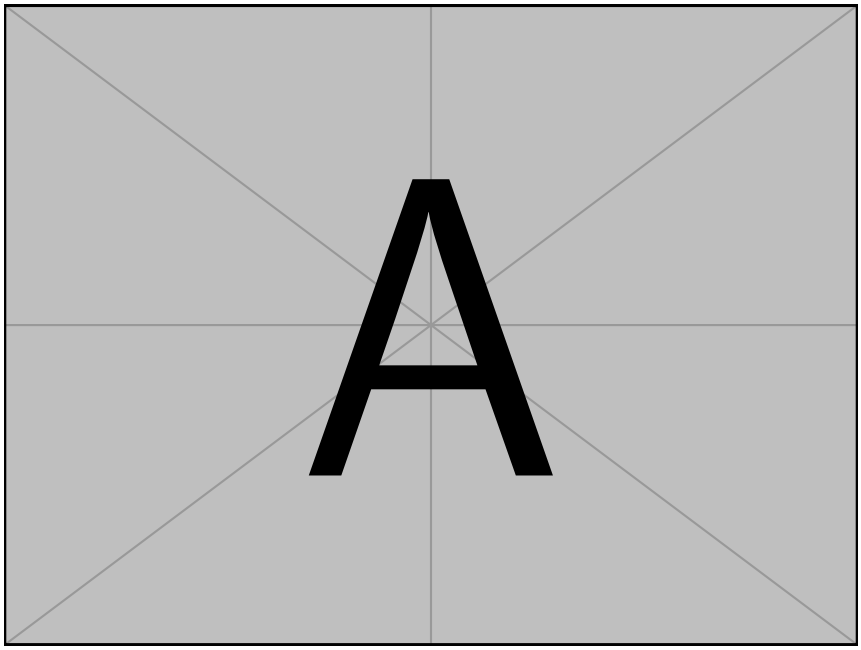

Figure 1.3: Caption

1.1.4 Large-Scale Subsidence

The previous forms of subsidence tend to impact localised to regional areas of land, whereas other processes can effect much larger areas, effecting whole countries or continents. One such process is Glacial Isostatic Adjustment (GIA), which involves the slow, long-term rebound of the Earth's crust in response to the melting of thick ice-sheets that covered vast areas of the Northern Hemisphere during the last ice age [51]. The common observed effects of GIA are post-glacial rebound, which is seen in movements in the land surface; these movements are much slower than the other subsidence factors already discussed, and trigger changes in sea-level and solid-earth deformation at a scale of $\sim$100 m over tens of thousands of years [54].

1.1.5 Sources of Anthropogenic Subsidence

As previously mentioned, the majority of serious subsidence is as a result of anthropogenic activity. One of the most prevalent and wide-reaching forms of anthropogenic subsidence is as a result of mining. Some methods of mining, such as total-extraction methods, remove all of the mineral present which leaves an unsupported mine roof that is allowed to collapse; in these instances ground subsidence is inevitable and rapid, and can be predicted using empirical methods [53]. Other forms of mining don't remove all of the mineral, in which case uncertainties surround the eventual collapse of these areas and the ensuing ground subsidence. Moreover, ground deformation related to mining activity isn't solely as a result of the physical extraction of minerals, but also from the groundwater pumping that is required prior to, and during, mining activities. Following the cessation of mining activities, groundwater pumping is stopped, and the surrounding area can see uplift due to the groundwater rebound. These effects are common in Britain, and have reported uplifts of 1 cma^{-1} in South Wales [23] and regional-level uplifts in Durham and Northumberland [38] following

mine closures.

Additionally, cities present a myriad of combining factors that contribute to subsidence. For instance, many cities are built near coastal deltas or river estuaries; in these cases the ground surface often contains a high proportion of unconsolidated sediments, such as clay, silt, and sand, which are susceptible to subsidence. The construction of buildings and streets adds to the stress exerted on the soils, and the drainage required for construction, coupled with groundwater extraction for human consumption and industrial use, results in hydro-compaction and a lowering of the water table [57]. These components have lead to a considerable number of cities throughout the world facing problems due to subsidence and relative sea-level rise.

1.2 Measuring Subsidence

Traditional ground-based methods of monitoring land subsidence is typically carried out through field-work, with the use of instruments such as spirit-levels, geodimeters and extensometers [13]. In general, measurements from these devices will be highly accurate, however they have low-spatial resolution and require a trained operator to generate the readings (therefore requiring a high-cost of labour). Other ground-based solutions, such as continuous GNSS stations, remove the need for a human expert to operate the devices, and deliver observations with very high temporal resolution. However, GNSS networks are usually sparse and rely upon spatial interpolation to provide continuous measurements across an area. Additionally, the stations need to be physically installed, and therefore the recorded measurements are only of known areas (i.e. they won't pick up instances of unexpected subsidence in areas they aren't monitoring). For these reasons, spaceborne methods of monitoring have become more common.

1.2.1 Synthetic Aperture Radar

Developed from Side-Looking Airborne Radar (SLAR), Synthetic Aperture Radar (SAR) is a form of imaging radar system that utilises a side-looking radar to sequentially transmit chirped pulses of microwave radiation and measure the reflected signals. The basic operation of the radar system involves determining the range distance R from the radar to a point scatterer on the ground (which is related to the echo-delay between the transmitted and received radar pulse), and is achieved by calculating

$$R = \frac{c\tau}{2} \tag{1.1}$$

where c is the speed of light, τ is the radar pulse length, and the factor $\frac{1}{2}$ is used to account for the 2-way transmission and reception of the signal [56].

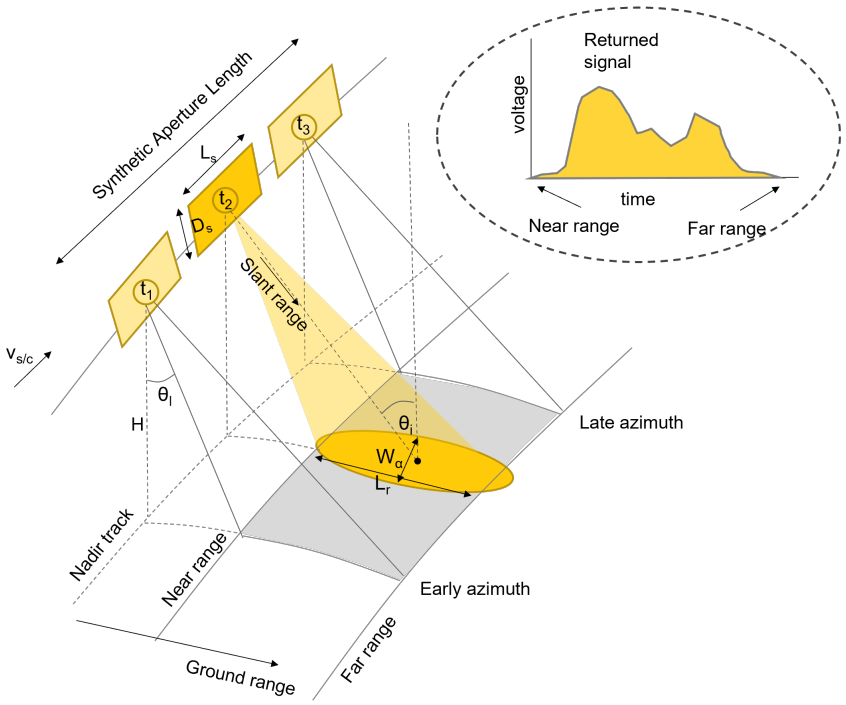

Figure 1.4: Simplified SAR acquisition geometry, adapted from [40] and [52].

Figure 1.4 displays a simplified geometric overview of the data acquisition process for a spaceborne SAR satellite. A satellite travelling with velocity v_s/c at a near constant height H over nadir, pointed at a look angle θ_l perpendicular to the along-track satellite flight path (known as the cross-track or *range* direction), emits radar pulses which illuminate an area on the ground surface. Successive radar pulses sweep across the ground swath from near range to far range, and the time delay between the backscattered signals correspond to the differences in slant range between the satellite and ground targets within the antenna footprint (with reflections arriving sooner from the near range than far range). The antenna footprint has dimensions W_a in the along-track (or azimuth) direction and L_r from near to far range (known as the swath width). These are given by:

$$W_a = \frac{\lambda}{L_s} R \tag{1.2}$$

$$L_r = \frac{\lambda R}{L_s cos^2(\theta_i)} \tag{1.3}$$

where R is the slant range from the satellite to the ground target, and θ_i is the incidence angle from the ground target to the local normal. For real aperture radar (RAR), this is the maximum azimuth resolution achievable [40], which corresponds to approximately 3.1km for Sentinel-1. However, in contrast to earlier airborne radar systems, SAR is a coherent system that retains both the amplitude and phase information of a returned radar pulse. This enables a significant increase of the azimuth resolution by capturing multiple returned signals using a moving antenna to simulate the effect of a much longer physical antenna, synthesising a large aperture [40]. The resolution in range and azimuth are focused using processes including range modulation and compression, Doppler Centroid filtering, and matched filtering; the result of which increases the spatial resolution of a SAR resolution cell to the order of meters. Each pixel in the

resulting SAR image contains the superposition of returns from all elemental scatterers within a SAR resolution cell; this leads to different amplitudes in neighbouring pixels, and results in a characteristic speckle effect.

1.2.2 SAR Interferometry

In addition to the amplitude, each pixel contains the coherent sum of phase returns from the elemental scatterers. SAR interferometry (InSAR) calculates the difference in phase between two or more SAR images to determine a difference in range as a proportion of the radar wavelength; as the wavelength is in the scale of centimeters (~5.6 cm for Sentinel-1) this can yield precise millimetric changes in the surface elevation. Radar images used for InSAR can be from mutually displaced flight tracks (cross-track interferometry) or from the same flight track but acquired at different times (along-track interferometry) [46].

Across-track interferometry is typically used to generate Digital Elevation Models (DEMs) that measure the surface topography. A single SAR image doesn't contain information about the elevation angle, and thus height information can't be retrieved; a second acquisition measured from a different perpendicular baseline can resolve this limitation, and calculate the height difference proportional to the range difference:

$$\Delta r \simeq \frac{\beta_\perp}{r_0 sin(\theta_i)} \Delta h \tag{1.4}$$

where r_0 is the slant range, θ_i is the local incident angle, and $\beta_\perp$ is the baseline perpendicular to the line of sight [46], see Figure 1.5 for a graphical example. For coherent radars, Δr corresponds to a measured phase difference $\Delta\varphi$:

$$\Delta\varphi = m\frac{2\pi}{\lambda}\Delta r \tag{1.5}$$

where λ is the carrier wavelength and m is a factor equal to 1 or 2 depending on whether it is a single-pass or repeat-pass interferometer [46].

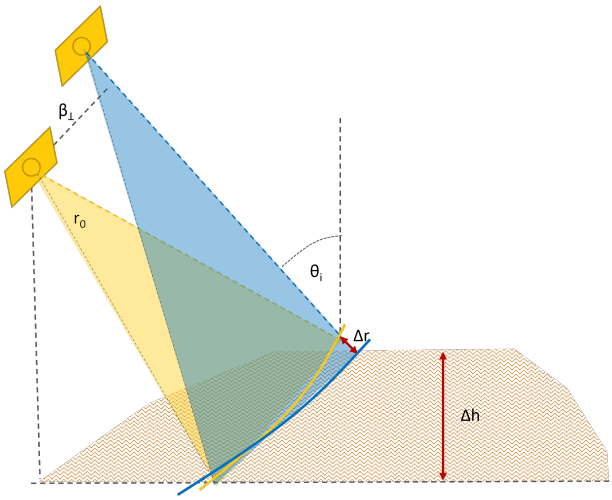

Figure 1.5: r_0 is the slant range, θ_i is the local incident angle, and $\beta_\perp$ is the baseline perpendicular to the line of sight. Adapted from [46].

To generate the DEM from the SAR acquisitions a couple of processing steps are

needed; the images are co-registered, which aligns the pixels between the two images so that they map onto the same ground surface points; the co-registered images are then cross correlated to produce an interferogram and the flat-earth contributions are removed by subtracting the expected phase contribution, utilising a reference surface; finally, the flat-Earth corrected interferogram is unwrapped, which converts the phase difference values, to the absolute phase differences, which can be used to infer the pixel heights [56].

Differential InSAR

Differential InSAR (D-InSAR) aims to measure the change in ground surface elevation between two SAR images acquired at different times. Changes to the surface elevation are represented as a proportional change in the interferometric phase $\Delta\phi$, which is independent of the perpendicular baseline and given by:

$$\Delta\phi = \frac{4\pi}{\lambda}d \tag{1.6}$$

where d is the relative scatterer displacement projected in the slant range direction [34]. Generally, the two SAR acquistions are made from different locations in space as well as at different times; this means that the resulting interferometric phase will have both topographic and surface deformation phase effects. Additionally, other phase contributions from atmospheric conditions will also be present. To accurately measure the deformation effects, these other effects must be carefully considered and accounted for in the InSAR processing steps to limit the error introduced to the deformation signal.

1.2.3 InSAR Limitations

Although InSAR has proven to be a very effective way of measuring ground deformation at scale, there are some limitations with what areas it can measure.

Geometric Distortions

Due to the side-looking geometry of the SAR antenna, geometric distortions can be present in the SAR imagery. This occurs where surface slopes significantly diverge from which the slant range data are projected; the result of this is foreshortening, where the slopes that are facing the SAR antenna appear narrower and slopes facing away are elongated, and in extreme cases layover, where the peak of the slope appears closer to nadir than the base [56]. These effects can cause issues during the phase unwrapping process. Related to this is shadow, which typically appears in mountainous regions, where sections of the surface are obscured from the microwave signal as a result of nearby peaks casting a shadow away from the radar system. The impact of this is gaps in the data where the microwave signal is unable to reach.

Coherence Loss

The principles of InSAR rely upon the coherence of the backscattered signal from elemental scatterers through time and space; if the signals between acquisitions decorrelate (lose coherence) then the resulting calculations to measure deformation won't

work. Generally, signals decorrelate when the properties of the ground scatterers significantly change between acquisitions; this could be due to the rapid changing nature of the scatterers or from large temporal baselines between acquisitions. The result of this is that areas of land cover that undergo lots of change, such as vegetated areas, have lower densities of coherent pixels and can't be reliably measured. Some multi-temporal InSAR approaches, such as Intermittent Small Baseline Subset (ISBAS) [48], aim to increase the density of measurement points in these areas by considering pixels that are discontinuously coherent throughout the entire InSAR time-series image stack.

Phase Unwrapping

Phase unwrapping is a key component of the InSAR processing chain, which involves unwrapping the wrapped [-π, π) phase measurements to an absolute phase signal. Phase unwrapping can introduce errors into the deformation signal which result in an offset in the deformation signal; some phase-unwrapping methods, such as least squares, can propagate these errors throughout the entire image [40].

1.3 Mapping Subsidence

1.3.1 SubCoast

Developed as part of the European Union's 7th Framework Programme for Research (FP7), SubCoast was a project delivered by BGS and several other European agencies with the aim of providing an integrated GIS product to highlight subsidence hazards in low-lying coastal zones around the European coastline [24]. The main output of the product was a 1km^2 gridded dataset which, amongst other factors, included the likelihood of subsidence and Relative Sea Level Rise (RSLR) for coastal lowland areas. Subsidence risk values were calculated for each grid cell by interpolating PSI data, and supplementing with geological data where PSI wasn't available. SubCoast utilised geological lithologies from OneGeology Europe, PSI data from Terrafirma [25] and interpretations from PanGeo [7] to focus only on areas of observed motion, to discriminate natural subsidence against anthropogenic processes.

Deposit	Litho_1/2	Litho_3/4	Litho_5
Peat	90	60	30
Organic Rich	70	47	23
Sapropel	50	33	17
Ooze	50	33	17
Clay	33	22	11
Mud	19	13	6
Claystone	6	4	2
Diamicton	20	13	7
Mudstone	4	3	1
Lignite	25	17	8
Silt	5	3	2
Sand	2	1	1
Shale	5	3	2
Wacke	1	1	0
Salt	100	67	33
Gypsum	100	67	33
Anhydrite	100	67	33
Other	0	0	0

Table 1.1: PSP values for deposit types in the OneGeology dataset. Each value represents the maximum percentage each deposit could decrease in volume by, depending on the 'Litho category'. Adapted from [42].

Following this, the methodology was adapted to derive the Potential Subsidence Rates (PSR) for rock classifications across the whole of Britain. OneGeology lithologies that were susceptible to subsidence from dissolution, compaction, or shrinkage, were assigned values representing the potential percentage change each lithology could undergo due to these processes. The percentage volume decrease, or Potential Subsidence Potential (PSP), was calibrated against the interpreted PSI velocities from areas within 10 cities in Europe that were undergoing natural subsidence due to these processes to derive the PSR on a scale of millimeters [42]. The PSPs for OneGeology lithologies were mapped to the BGS Rock Classification Scheme (RCS), by combining the 1:50k superficial and bedrock geology maps of Britain, resulting in a finer resolution map of PSPs. For each polygon in the combined superficial and bedrock map, the overall PSP was determined as an overriding process from either the bedrock or superficial deposits based on the thickness of the superficial deposit layer, using the logic specified in Table 1.2. The overall PSP was used to derive the PSR for each polygon, based on the relationship between PSP and PSR derived in the calibration process.

Superficial thickness [m]	PSP Basis
0 (no superficial deposit)	Bedrock
[1-3)	Max. of Superficial or Bedrock
[3-5)	IF Bedrock PSP >= 25% THEN max. of Superficial or Bedrock ELSE Superficial
>5	Superficial

Table 1.2: The logic used to define the basis for assigning PSP values based on the superficial geology thickness and PSP values. Adapted from [42].

1.3.2 National-scale Subsidence Monitoring

The wide-spread coverage and availability of high resolution SAR images, from missions like Copernicus Sentinel-1, together with advances in InSAR processing algorithms, have enabled the monitoring of land subsidence on a national and continental-scale [30].

1.3.3 EGMS

Launched in 2022, the EGMS is part of the Copernicus Land Monitoring Service and includes natural and anthropogenic ground motion velocities at local, regional, and continental scales. Following on from the national-level surveys of Germany, Denmark, Norway, The Netherlands, and Italy, the EGMS is the largest GMS in Europe, and the first application of InSAR technology to monitoring ground deformation over an entire continent [29]. Utilising a combination of multi-temporal Persistent Scatterer and Distributed Scatterer InSAR processing algorithms applied to full-resolution Sentinel-1 SAR imagery, the EGMS contains the historic deformation of ground Measurement Points (MP) for all Copernicus member states in Europe. The current data archive spans between February 2015 to December 2021, and will be updated in September 2023 to include measurements between January 2018 and December 2022 [8]. Going forwards, the service will be refreshed annually, providing a 5-year window of data.

The ground motion data is packaged into three products [8]:

- **Basic** - Line of sight velocity maps in ascending and descending orbits, referenced to a local reference point.
- **Calibrated** - Line of sight velocity maps in ascending and descending orbits referenced to a model derived from global navigation satellite systems time-series data.
- **Ortho** - Components of motion (horizontal and vertical) anchored to the reference geodetic model, resampled to a 100 m grid.

As the basic products are spatially referenced to a virtual reference point, the provided measurements are only meaningful within the processed area; comparisons of deformations between adjacent areas are not possible as each area is referenced to a different scale. The calibrated products are fundamentally the same as the basic product, but the InSAR MPs are referenced to a model derived from GNSS time-series data, which provides absolute values of the displacement velocities. This enables the comparison of deformation signals between adjacent areas belonging to different products of the same level [28]. For both the basic and calibrated product, the ground motion data is provided in two datasets; one for velocities derived from observations acquired from the satellite's ascending pass, and another from the descending pass. In contrast, the Ortho product provides measurements that aren't in the satellite line of sight, but are re-projected into purely vertical and horizontal (east-west) directions by exploiting the satellite look angle. MPs from the ascending and descending geometries of the calibrated product are gridded to 100m and grid cells without both ascending and descending observations are ignored. Due to the near-polar orbit of Sentinel-1, the InSAR measurements aren't sensitive to motion in the north-south direction; rather than

assume no displacement, any north-south component is removed from the InSAR data by re-projecting north-south motion derived from GNSS measurements to the satellite line of sight and subtracting this from the calibrated product. The ascending and descending MPs within each grid cell are then separately averaged and decomposed to give the vertical and east-west displacements [35]. This is summarised in Figure 1.6.

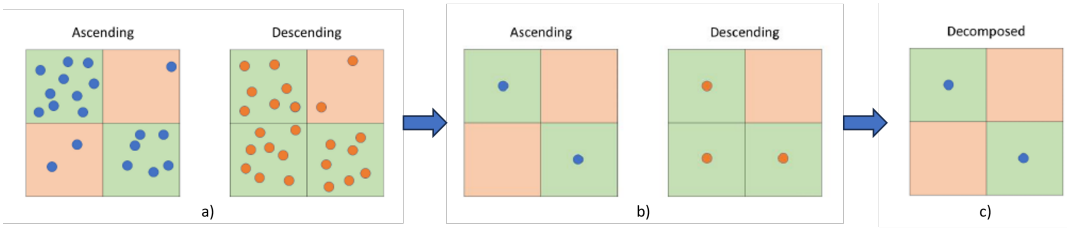

Figure 1.6: Overview of the Ortho decomposition process. (a - b) Ascending and descending MPs in each grid cell are averaged, and only cells which meet a minimum number of MPs are retained. (b - c), cells with both an ascending and descending MP are decomposed to give the vertical and east-west displacements. Source: [35]

The outputs from EGMS are freely available to download from the EGMS web portal[1]. The web interface provides an easy way to view, analyse, and download ground motion data for an area of interest, and includes a view of the historic deformation time-series data and trend for each measurement point as well as the average deformation time-series for a specified region (see Figure 1.7).

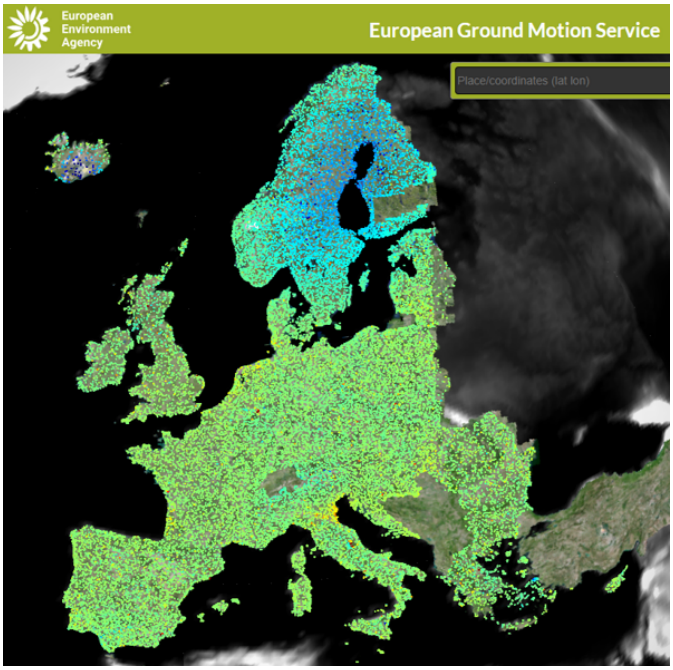

(a) EGMS web portal landing screen

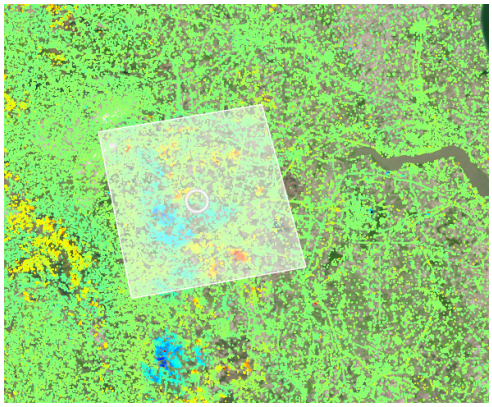

(b) EGMS point average tool

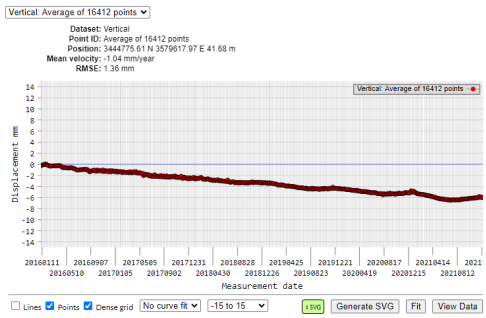

(c) Average velocity graph

Figure 1.7: The historic deformation for each measurement point contained in EGMS is able to be viewed in the web platform. An average of several measurement points is computed using the 'compute average' tool and selecting a polygon of points in an area of interest (b). The deformation time-series from each point/collection of points is able to be viewed as well as fitting a linear, logarithmic, or polynomial trend (c). The graph can be exported to SVG and the data points for the graph can also be viewed and copied to another programme for quick analysis.

[1]https://egms.land.copernicus.eu/

With this, the EGMS is suitable for monitoring a wide range of geohazards including natural and anthropogenic subsidence, landslides, tectonic motion, and volcanoes [44]. The outputs from EGMS are available to be used in downstream applications and analyses, but, at the time of writing, haven't been utilised in many studies to date [43, 47], likely due to the relative recency of the service. With new developments of value-added products enhancing the ease of data acquisition and conversion [36], as well as attempts at automatically detecting and classifying areas of significant motion [9], projects utilising EGMS for large-area ground displacement should become more common in future. For countries like the UK, which had no freely-available national GMS capability prior to the launch of EGMS, this creates the potential for measuring the land subsidence time-series and extracting the underlying natural and human causes on a scale which hasn't been done previously.

Chapter 2

Methodology

In this chapter, the design and development of various stages of the project are specified. An outline of the main processing steps and analysis methods are included, as well as an overview of the software used to conduct the analysis, and summaries of the input datasets are presented.

2.1 Project Design

2.1.1 Software Tools

The majority of the data processing and analysis for this project was conducted using python 3.9, utilising the associated geospatial and data analytics libraries (GeoPandas, NumPy, Shapely etc). Python was chosen as the programming language due to the familiarity, ease of development, and to keep the project as open source as possible. Furthermore, using python over traditional GIS applications like ArcGIS or QGIS has the benefit of documenting the analysis workflow in a step-by-step manner, which increases the reproducibility of the analysis, in addition to offering a greater level of customisation and better data processing capabilities. The work was split into three main notebooks, each considering a particular aspect of the project:

1. *egms_data_processing.ipynb* - this notebook contains the processing steps for the raw EGMS and SubCoast data.
2. *egms_subcoast_data_exploration.ipynb* - this notebook contains the majority of exploratory data analysis and analytical work comparing the EGMS and SubCoast datasets for Britain.
3. *london_case_study.ipynb* - this notebook contains the analysis for the London case study.

Common visualisation and analysis functions were contained in separate python scripts and imported into each notebook to improve the overall readability, by keeping the focus on the analysis rather than function definitions. These included:

- *config.py* - this python script contains the file directories for data, outputs, temp files, and is imported into each notebook.
- *generalfuncs.py* - this python script contains general data processing functions

used in many aspects of the project.

- *mapfuncs.py* - this python script contains the custom mapping functions used for map plots.
- *graphfuncs.py* - this python script contains the custom graph functions used for graphical plots and charts.

All notebooks and scripts, as well as the specific python environment configuration, are available on GitHub[1].

2.1.2 Project Overview

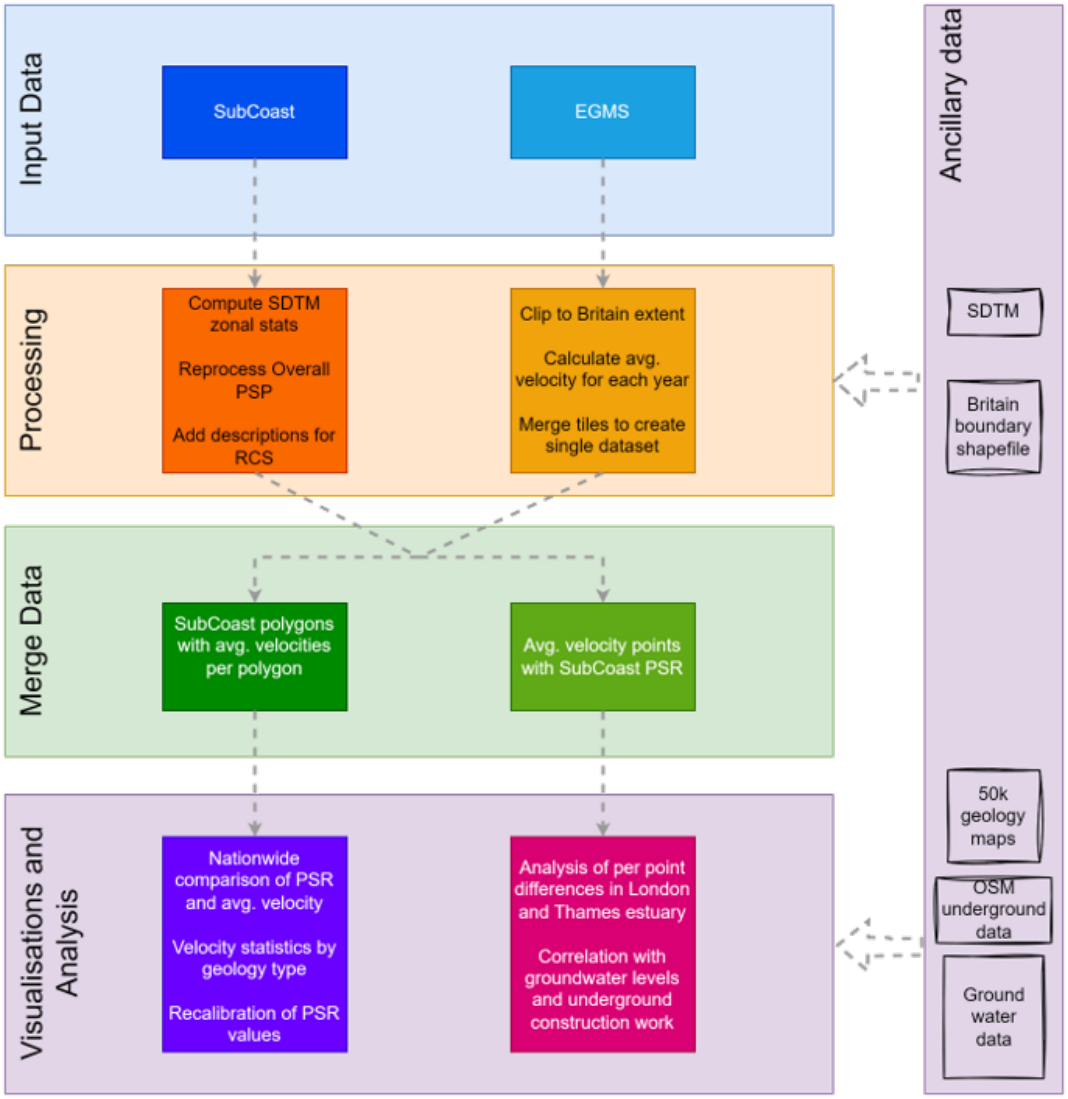

Figure 2.1: Stages of the data workflow. The project is primarily concerned with the integration of SubCoast and EGMS data; other datasets used in the analysis are included in the ancillary data. More information on the specific processing for each dataset are included in Section 2.4.

Figure 2.1 gives a summary of the main stages of the project development. The main aspect of the analysis entails integrating the SubCoast and EGMS data to create a com-

[1]https://github.com/DavidFountain/mres-project

bined dataset, from which comparisons between PSR and average velocity and other simple analyses can be undertaken. Separate data cleaning and processing are applied to each dataset before spatially joining, which creates two individual datasets; one that is grouped by SubCoast polygon with average EGMS velocities per polygon, and another grouped by EGMS point with the corresponding PSR values. From these datasets, an overall analysis for the extent of Britain and a more detailed view of the London Thames area can be conducted. Further detail on the processing steps follows in the upcoming sections.

2.2 Input Datasets

Dataset	Source	Format	File Size	Description
SubCoast	BGS	.gdb	2.43 GB	The SubCoast geodatabase contains the polygon shapefile for Potential Subsidence Rates (PSR) in Britain, with each polygon designated a corresponding bedrock and superficial rock classification scheme (RCS) value. Additionally, there are mapping files which give the full text description for each RCS code, and the Potential Subsidence Potential (PSP) for each RCS.
EGMS Ortho Vertical Product - Britain	EGMS	.csv	10.5 GB	The EGMS data contains the vertical InSAR ground displacement time-series for Britain. The data is contained within 51 individual .csv files (ranging from 2.3 to 923 MB for each individual file) which are geocoded to represent the centre point of each 100x100 m grid cell.
Superficial Deposit Thickness Model	BGS (via EDiNA DigiMap service)	.tiff	1.1 GB	The advanced superficial thickness model contains the thickness of superficial deposits across Britain, in a geo-tiff file with a pixel resolution of 50 m.
Borehole Water Levels - London	BGS	.csv, .shp	23.3 MB	Water level information for 69 boreholes in the Greater London area, measured in Metres Above Ordnance Datum (mAOD) which is based on the mean sea level height. The data contains individual .csv files for each borehole and a .shp file containing the location of each borehole.
Mining Hazards - Britain	BGS	.shp	39.9 MB	1 km hex grid dataset indicating the likelihood for mining to have occurred (excluding coal mines). The data contains 3 classifications of likelihood; low, medium, high. Areas with no record of activity have n/a values.
London Underground Stations and Line	Open Street Map	.shp	635 MB	Point data showing the locations of London underground stations, and Lines indicating the underground tunnel routing. The OSM data is volunteered information, which means that the accuracy of locations can't be guaranteed.
1:50k Superficial & Bedrock Geology Maps - Britain	BGS (via EDiNA DigiMap service)	.shp	4.2 GB	1:50k scale geology maps of Britain, indicating the superficial and bedrock deposits in each polygon. In addition to the SubCoast data, these maps contain more information about the types and ages of lithologies.

Table 2.1: Summaries of the main data inputs used in this project. The file sizes are given for the full unprocessed data, which were considerably reduced once the data had been processed and the necessary attributes were extracted.

2.3 Analysis Methods

As stated in Section 0.3, the purpose of this project is to investigate the differences between PSR and average velocity between the SubCoast and EGMS datasets, with the purpose of identifying areas of similar/differing movement and relating the causes of motion to the underlying geological processes and anthropogenic activities. To achieve this, very simple statistical analyses of the average velocity were made between different geological deposits and areas of known anthropogenic disturbance - including groundwater discharge, mining, and underground construction works. This was facilitated by the integration of several datasets, as outlined in the previous section.

To compare the differences between overall PSR and average velocity, only areas with a PSR < 0 mma^{-1} and average velocity <= 0 mma^{-1} were considered. This is because the SubCoast data only considers subsidence, so directly comparing areas of uplift doesn't make sense. Furthermore, areas with 0 PSR denote lithologies which aren't susceptible to the subsidence stemming from dissolution, compaction, and shrinkage, so, again, the comparisons between SubCoast and EGMS in these areas doesn't have much meaning.

To recalibrate the PSRs based on the updated EGMS ground motion velocities, different measures of the average velocity for each PSP value was computed and compared. Consistent with methods used in the original SubCoast study [42], the weighted mean EGMS velocity was computed for each distinct PSP value, with the assumption that polygons with a greater number of MPs will give a more robust mean velocity. Additionally, unstable MPs, defined as subsiding more than $\mu - 2\sigma$, were removed from the data and the maximum subsiding values were compared with PSR (as PSR is a measure of the theoretical maximum annual subsidence rate, which is likely to be significantly different to the average rate). MPs below $\mu - 2\sigma$ were removed as these could represent points of anthropogenic influence, or possibly measurement errors, which could introduce noise into analysis if maximum subsidence values were compared directly.

After comparing the correlation between PSP and average velocity, a linear regression model was fit to the data points in the form $PSR = \beta_0 \times PSP$ to get the potential subsidence rate as a measure of PSP. Again, this is following the methodology as set out in the original SubCoast PSR derivations [42].

2.4 Data Processing

This section describes the data processing steps introduced in the above sections in more detail. Primarily, this is in regards to the SubCoast, EGMS, and combined datasets.

2.4.1 SubCoast

The SubCoast dataset was provided as a shapefile by BGS, and covers the entire landmass of Britain with a total area of 234,990 km^2. The data contains 6,531,297 polygons,

each with a designated PSR and both the individual superficial and bedrock RCS and PSP values, in addition to the overall PSP used for the PSR calculation (an example of the data is included in Table 2.2).

gridcode	SUP_RCS	BED_RCS	SUP_PSP	BED_PSP	OverallPSP	OverallPSR
1.0	XCZSV	GN	33.0	0.0	33.0	-2.591
0.0	S	GN	2.0	0.0	0.0	0.0
1.0	S	GN	2.0	0.0	2.0	-0.157
3.0	S	GN	2.0	0.0	2.0	-0.157
5.0	S	GN	2.0	0.0	2.0	-0.157

Table 2.2: SubCoast data extract. SUP/BED_RCS are the RCS codes for superficial and bedrock geology types, and SUP/BED_PSP are the respective percentage volume decrease potential. OverallPSP and OverallPSR are the overall PSP and PSR values used for each polygon, and are determined from either the bedrock *or* superficial values. E.g. cells highlighted in orange show where SUP_PSP has been used for OverallPSP, whereas row two uses BED_PSP.

Including areas of no subsidence, there are 12 distinct values for PSP/PSR ranging from 0 to -7.065 mma^{-1} (0 to 90 PSP) with 42.5% of the area within the range -0.471 to 0 mma^{-1}, and most areas subsiding by either -1.57 mma^{-1} (24.6%) or -2.59 mma^{-1} (23.1%). As highlighted in section 1.3.1, the overall PSP is derived from either the superficial PSP *or* bedrock PSP, depending on the thickness of the superficial deposit layer (see Table 1.2). However, the dataset doesn't include a column that specifies the geological basis for the overall PSP; to determine this, the bedrock/superficial RCS was input where the overall PSP equalled the corresponding bedrock/superficial PSP. Using this logic 491,130 polygons (7.52% of all polygons and 5.52% of the total area) weren't attributed to a single RCS value, as both the superficial and bedrock PSP were identical but their RCS differed. For these instances, the average superficial deposit thickness was calculated for each polygon by integrating the BGS Superficial Thickness Model with the SubCoast data. The same logic was then applied as in Table 1.2 to determine the source of the overall PSP. This reduced the number of ambiguous polygons to 244,542, and resulted in 2,670,699 polygons (40.89% of all polygons and 46.41% of the total area) attributed to superficial geology and 3,608,261 polygons (55.25% of all polygons and 50.68% of the total area) attributed to bedrock. The steps for this process are summarised in Figure 2.2.

The remaining data processing stages included joining the RCS descriptions to the dataset, and adding the OneGeology supergroups as outlined in Table 1.1. The supergroups were identified by matching the Litho_1-5 PSP values in Table 1.1 with the overall PSP values in SubCoast, and then finding the related RCS descriptions that included the OneGeology deposit names. The OneGeology classifications are used to group various lithologies across Europe, and, as such, not all classifications were represented in the data (e.g. Lignite isn't in the SubCoast data but Chalk is, which also has a PSP of 25). The outcome of this meant that the groupings were slightly different compared with those in Table 1.1. Furthermore, to better understand and measure the interaction of different geologies, *Sand* and *Sandstone*, and *Silt* and *Siltstone*, were split into separate categories where they had previously been categorised as *Sand* and *Silt* respectively. To differentiate these groupings between the 1:50k superficial and bedrock RCS names, the variable name *Geology Supergroup* was adopted.

PSR	PSP	Area (km^2)		
		Original	Reprocessed	Difference
0	0	30944	32043	1098
-0.079	1	28015	28023	8
-0.157	2	10945	11433	488
-0.236	3	3665	3665	0
-0.314	4	20659	35980	**15322**
-0.393	5	4359	4482	124
-0.472	6	855	880	24
-1.493	19	52	54	1
-1.572	20	57603	60414	2812
-1.965	25	10398	10405	7
-2.593	33	54160	34520	**-19640**
-7.073	90	13045	13091	46

Table 2.3: Comparison between the original SubCoast PSP/PSR distribution and the reprocessed data with the corrected Mudstone PSP values. The majority of the 19640km^2 difference has been put into PSP 4 (the corrected Mudstone value) with other large increases inPSP 20 and 0.

Upon reviewing the groupings, it became apparent that there was an error in the initial SubCoast data as deposits categorised solely as Mudstone (without any mix of Halite or Gypsum) were given a PSP of 33, which should have been either 4, 3, or 1. This error was confirmed by BGS, and subsequently the Bedrock PSP entries marked with Mudstone were changed from 33 to 4 and all overall PSRs were recalculated based on the relationship defined in Section 1.3.1 (see Table 2.3 for a comparison of the original and corrected PSP/PSR distributions). The steps outlined in Figure 2.2 were then repeated, which resulted in the overall PSP of 3,039,475 polygons (46.54% of all polygons and 49.95% of the total area) attributed to superficial geology and 3,416,498 polygons (52.31% of all polygons and 48.81% of the total area) attributed to bedrock. The number of ambiguous overall PSP polygons reduced to 67,529, and were excluded from further geological analyses.
Table 2.4 shows the final geology supergroups, along with their respective PSP and absolute and percentage coverage, with the spatial distribution displayed in Figure 2.3.

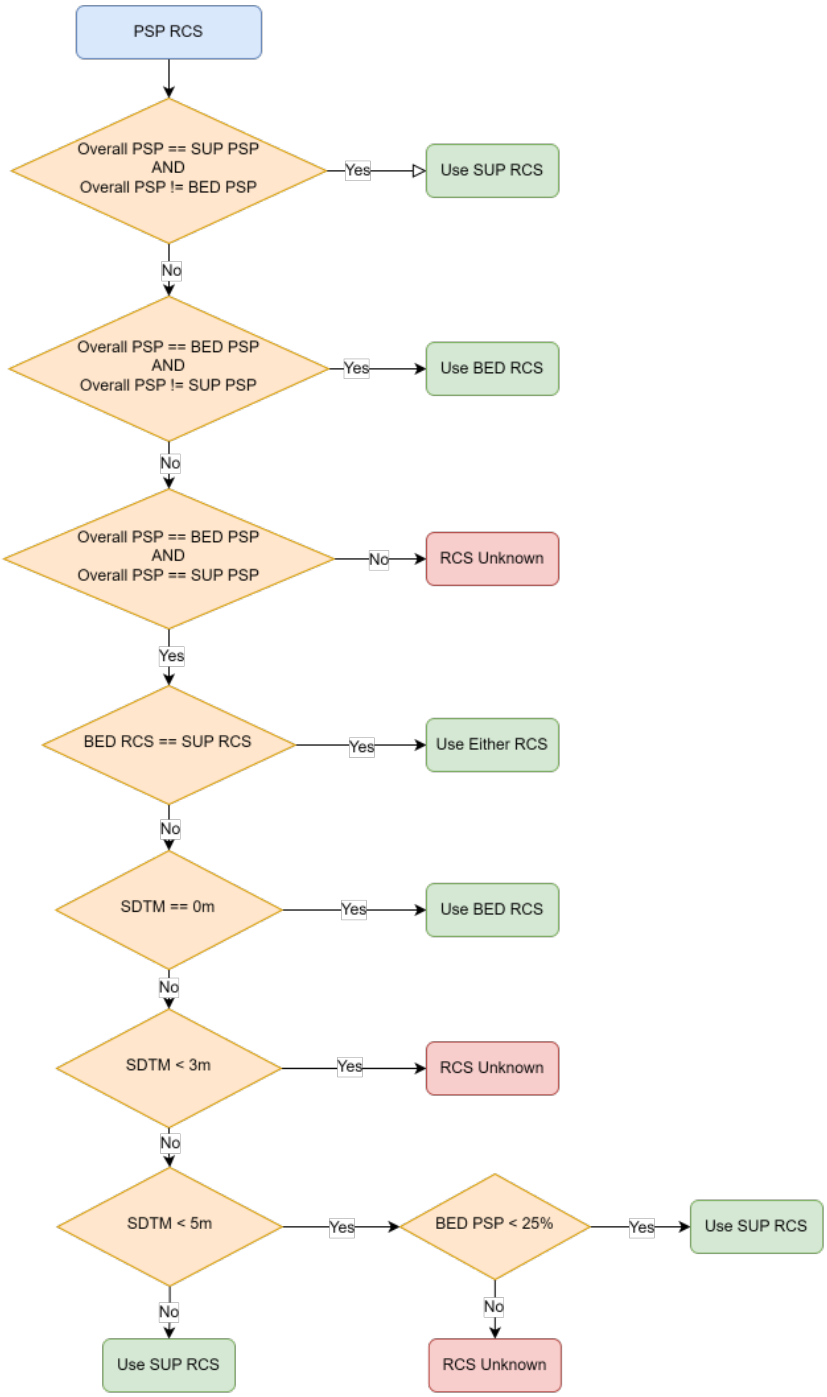

Figure 2.2: Flow chart depicting the steps in assigning an RCS description for the overall PSP value.

Geology Supergroup	OverallPSP	Count	Area (km^2)	% Area
OTHER	0.0	1233312	32042.55	13.75
WACKE	1.0	115945	3307.03	1.42
SANDSTONE	1.0	492141	17515.05	7.51
DIAMICTITE	1.0	1139	20.61	0.01
GRAVEL	1.0	6500	155.27	0.07
LIMESTONE/DOLOSTONE	1.0	168482	7024.72	3.01
SAND	2.0	257420	11433.24	4.9
SILTSTONE	3.0	101559	3665.22	1.57
MUDSTONE	4.0	919684	35980.21	15.43
SILT	5.0	134717	4482.34	1.92
CLAYSTONE	6.0	6405	879.65	0.38
MUD	19.0	1568	53.92	0.02
DIAMICTON	20.0	1513568	60414.48	25.92
CHALK	25.0	287339	10405.46	4.46
SALT	33.0	14959	843.57	0.36
CLAY	33.0	834743	31704.89	13.6
GYPSUM	33.0	2052	96.31	0.04
ANHYDRITE	33.0	30	0.15	0.0
PEAT	90.0	372205	13090.89	5.62

Table 2.4: Overall count of polygons and area covered by overall PSP and geology supergroup. Cells highlighted in blue groupings which aren't included in the OneGeology deposits.

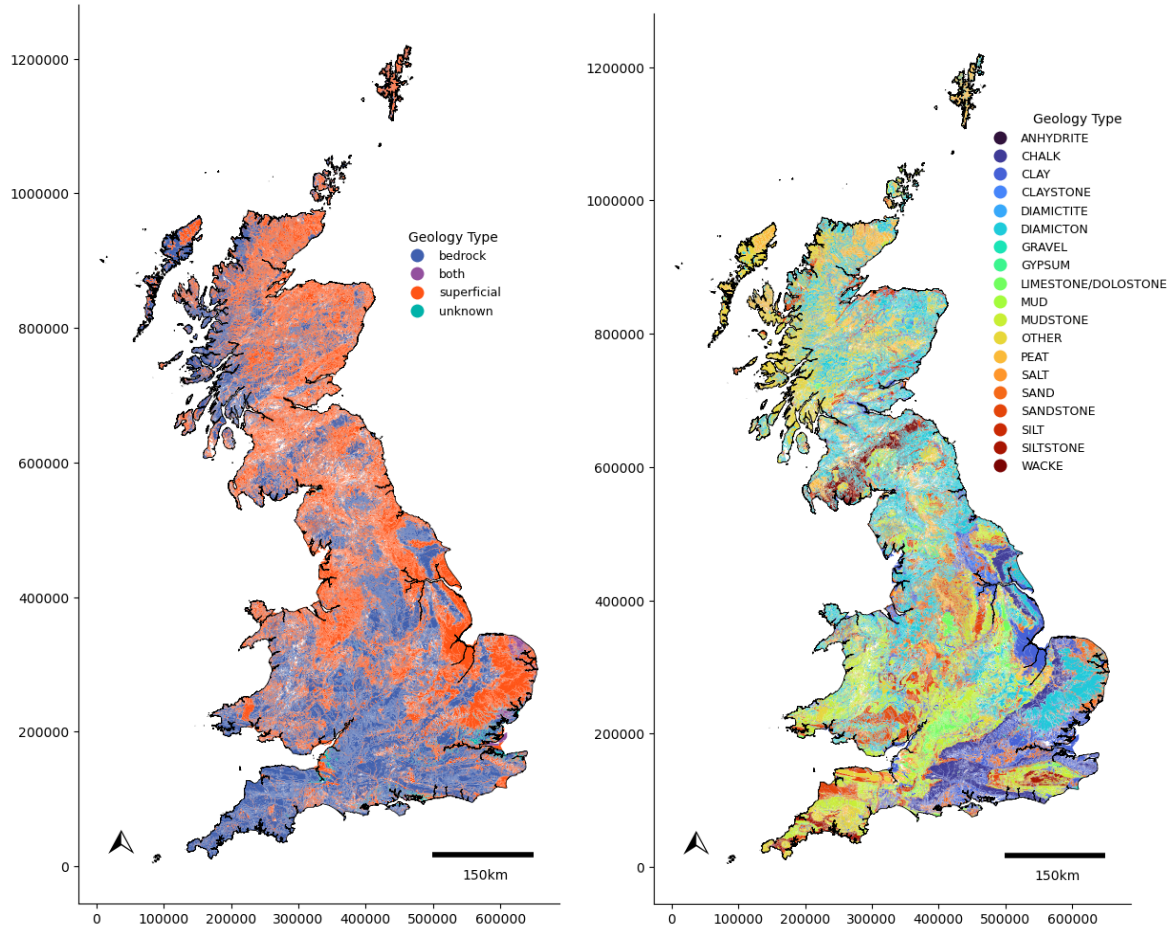

(a) PSP Geology Basis (b) Geology Supergroup

Figure 2.3: Maps showing the spatial distribution of a) geology basis for PSR calculation and b) geology supergroup throughout Britain. Areas classified as 'unknown' have the identical PSP values for both superficial and bedrock but different RCS, areas classified as 'both' have identical PSP and RCS values for superficial and bedrock.

2.4.2 EGMS

The EGMS data was downloaded from the EGMS web platform[2], selecting the Ortho Vertical Product. As previously described in Section 1.3.3, the dataset contains geocoded point data of the vertical ground displacement velocities, which is resampled to a 100m grid [44]. Data is disseminated in CSV file format, which cover predefined areas in discrete tiles (see Figure 2.5 for an example of the web platform and download functionality). To cover the extent of Britain, 51 individual tiles were downloaded with a range of 1,539 to 559,652 observations per file. These were merged to produce a single dataset, converted from the European coordinate reference system EPSG:3035 to British national grid (EPSG:27700), and clipped to the extent of Britain by intersecting the EGMS point data with the full-resolution boundary of Britain.

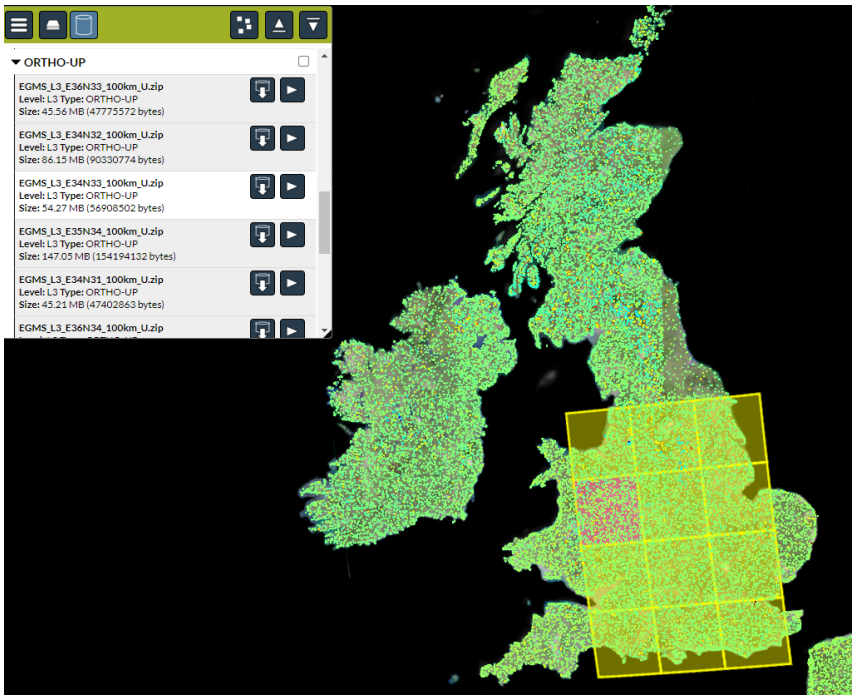

Figure 2.4: EGMS web portal download screen. Data can be downloaded in predefined tiles, with a maximum of two simultaneous downloads at any time.

Weekly time-series data are available for each measurement point (MP), which currently spans a 5-year time period from 2016-2021 (for the Ortho product), in addition to other metrics including the mean annual velocity and standard deviation (the full data specification is included in Appendix A.1). Although considerable historic data is available for each MP, for this analysis only the average annual velocities were considered (as these are comparable to the annual PSR in SubCoast). Additionally, this also has the benefit of considerably reducing the overall volume of data, simplifying the analysis and enabling it to be completed on a single laptop rather than employing distributed computing techniques. Therefore, to summarise the full time-series a first-degree polynomial was fit to each MP for each calendar year to derive the average annual velocity, and the individual weekly measurement columns were dropped from the dataset. This is similar with how the mean annual velocity is calculated for the

[2]https://egms.land.copernicus.eu/

full 5-year time period (specified in row 6 of Appendix A.1), which should allow for a comparison of deformation rates for each year.

After processing, the final dataset contained 6,245,563 MPs (of which 82% have an average velocity <= 0 mma^{-1}) with an average velocity of -0.83 mma^{-1} and a range between -72 to +65 mma^{-1}. As shown in Figure 2.6, the average velocity for the individual years varies between -0.68 mma^{-1} in 2016 to -1.0 mma^{-1} in 2021. The large scale trend of deformation rates over Britain shows the south is subsiding faster than Scotland and Northern England, with a mean subsidence in England of -1.15 mma^{-1} (standard deviation 1.09 mma^{-1}), compared to -0.48 mma^{-1} in Scotland (standard deviation 1.32 mma^{-1}).

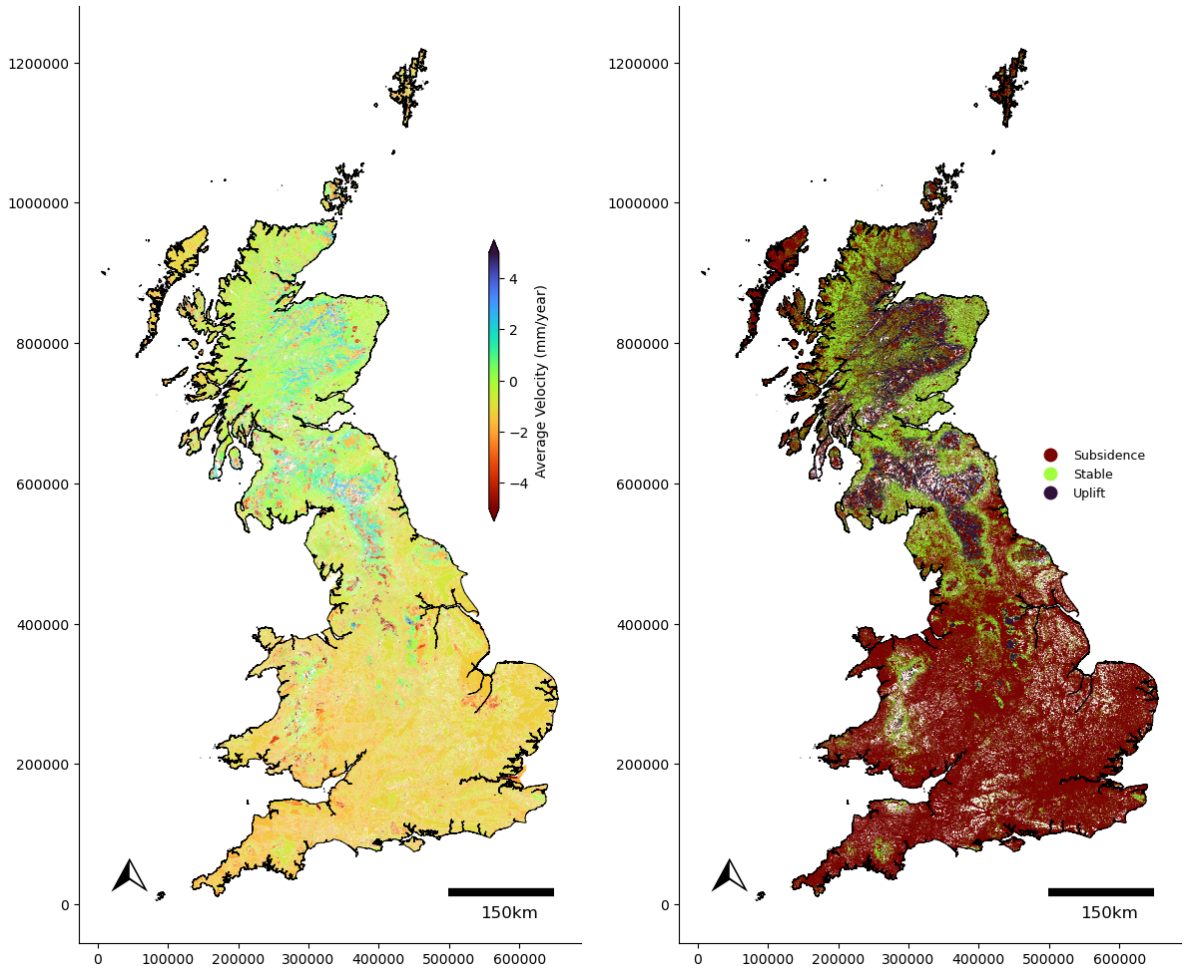

(a) Avg. Velocity (b) Avg. Velocity Classified

Figure 2.5: Average EGMS velocity across Britain. a) Negative values indicate areas of subsidence and positive values indicate areas of uplift. b) Classified map, categorizing areas with an average velocity < -0.5 mma^{-1} as subsidence, > 0.5 mma^{-1} as uplift, or otherwise stable.

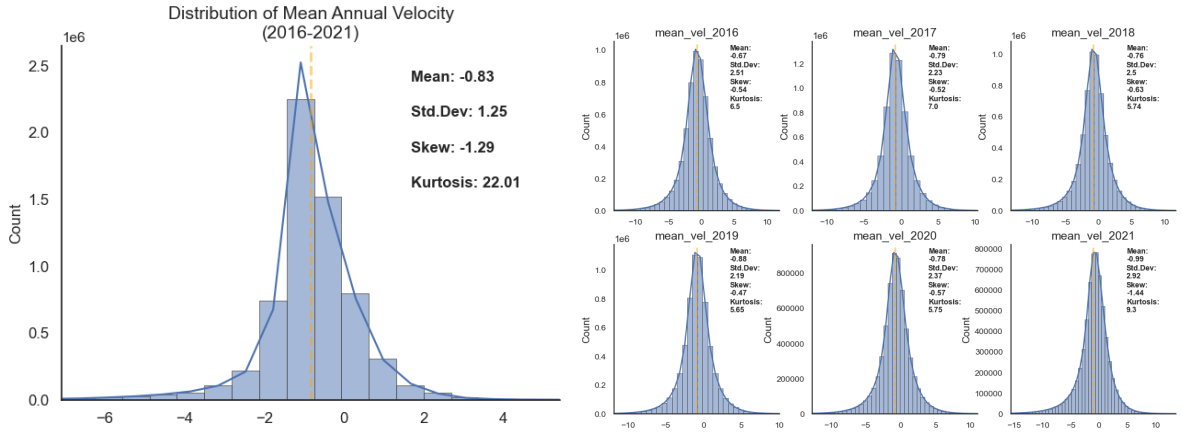

(a) Avg. Velocity 2016-2021 (b) Avg. Yearly Velocities

Figure 2.6: Distribution of EGMS velocities for a) the full 2016-2021 time frame and b) the individual years. The yellow dashed vertical line indicates the mean value.

2.4.3 Combined EGMS and SubCoast Dataset

After applying the specific processing steps to the SubCoast and EGMS data, the two datasets were joined together to produce a combined dataset from which the bulk of analysis was run on. This was accomplished as follows:

1. Spatially join the SubCoast and EGMS data where the SubCoast data contain the EGMS points. Make a copy of this dataset and write to disk.
2. Group by the SubCoast polygon index and aggregate all EGMS metrics for each SubCoast polygon.
3. Join the aggregated EGMS values back on to the original SubCoast data to get the average EGMS velocities per SubCoast polygon. Write the resulting dataset to disk.

The dataset created in step 1 is at EGMS point level; each row represents an EGMS point measurement, which has the corresponding SubCoast PSR and geology information attached. This dataset was used in the London case study analysis where the inter-polygon ground motion variations were considered. The dataset aggregated to the SubCoast polygon level was used to analyse the PSR and average velocity correlation on a national-scale.

The combined dataset includes 717,897 SubCoast polygons which have a minimum of one corresponding EGMS point contained within. This is a total of just 11% of the total polygons, however these polygons represent 86.6% of the total area, and 75% of the area contains an EGMS point with an average velocity <= 0 mma^{-1}. The polygons without an EGMS velocity are mainly found in Scotland and correspond to areas of land with high altitude, where the loss of data can be attributed to geometric distortions from shadows (as previously described in Section 1.2.1) or from low coherence due to snow cover.

2.5 London Case Study Area

The London case study considers an approximate 62 x 89 km area around Greater London, which extends from St Albans to Southend-on-Sea in the North and Surrey Hills to the North Downs in the South (see Figure 2.7), with a total area of 5,537 km^2. The study area is dominated by the London Clay Formation, which accounts for 46.3% of the area, and mainly comprises bioturbated or poorly laminated, blue-grey or grey-brown clay with varying levels of sand and silt, reaching a depth of up to 150 m in the eastern part of the London basin in Essex [4]. Areas of fine to coarse grain sand are distinguished within in the Bagshot Formation, with outer areas separated by clay, silt and fine-grained sand of the Claygate Member [5]. The Chalk Group accounts for 21% of the area, and spans a band from the south to west, with areas in central London and towards the Thames estuary, as well as in the north east towards St Albans. This is interspersed with the homogeneous, bioturbated, silty fine-grained sand of the Thanet formation, which ranges from 10-15 m thick in central London to 20-30 m in north Kent [6]. The lower region of the study area is comprised of cretaceous formations, mostly of mudstone (55%) and sandstone (11%), with interbedded limestone. The superficial deposits in the area mainly consist of pleistocene gravel members (22%) and poorly sorted and stratified superficial deposits (18%), with holocene alluvium deposits (15%) running along the Thames estuary (Figure **??**). The particular study area was chosen as it aligns with previous studies into the geological interpretation of ground deformation in London as measured by InSAR [20] and other mathematical modelling of groundwater abstraction [25], and the mechanisms of ground motion are well researched. In total, there are 246,494 EGMS measurements contained within the study boundary, with an average velocity of -1.25 mma^{-1} and a standard deviation of 0.68 mma^{-1}.

2.5.1 Additional Data

To measure the effects of potential human caused subsidence, auxiliary datasets were used to measure the correlations between the external factors and average velocity. These included the locations of the London underground network and stations, and groundwater level data from 69 boreholes. A 500m buffer was applied to the underground stations to measure the average velocity of EGMS points within these bounds. The groundwater level data contains the water level as a measure of Metres Above Ordnance Datum (mAOD), which is in reference to the mean sea level height. For each station, monthly measurements are included up until February 2021, and date as far back as January 2002. Additionally, each measurement has an associated quality classification that defines the characteristic of the measurement; for this project, all measurements with Good, Unchecked, Suspect, and Estimated qualities were included. The resulting dataset had 20,651 observations between January 2016 to February 2021, across 57 individual boreholes. The average number of observations for each borehole has high variance, with two boreholes having hourly measurements and others only a couple of measurements per year. The average water level was computed for each year between 2016 and 2020, and in a similar fashion to other studies linking ground deformation with groundwater abstraction [17, 18], the average groundwater level change was calculated by subtracting the 2016 levels from 2020. 2020 was used as the reference year due to only having data for January and February in 2021, and 32 of the stations missing 2021 measurements entirely. Boreholes with

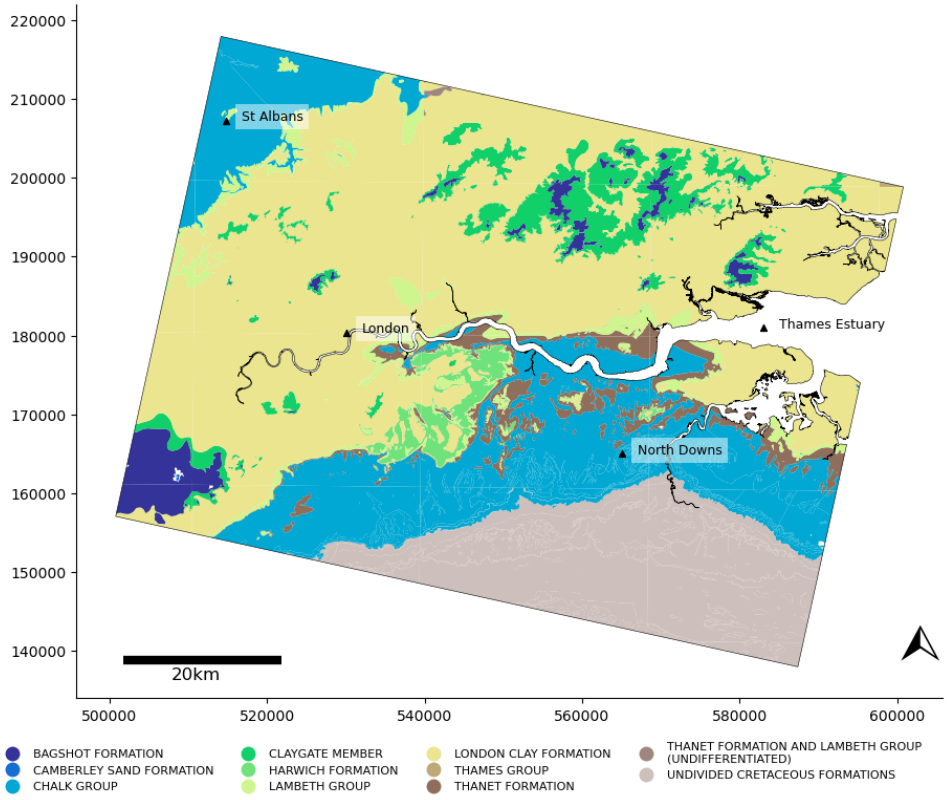

(a) Bedrock

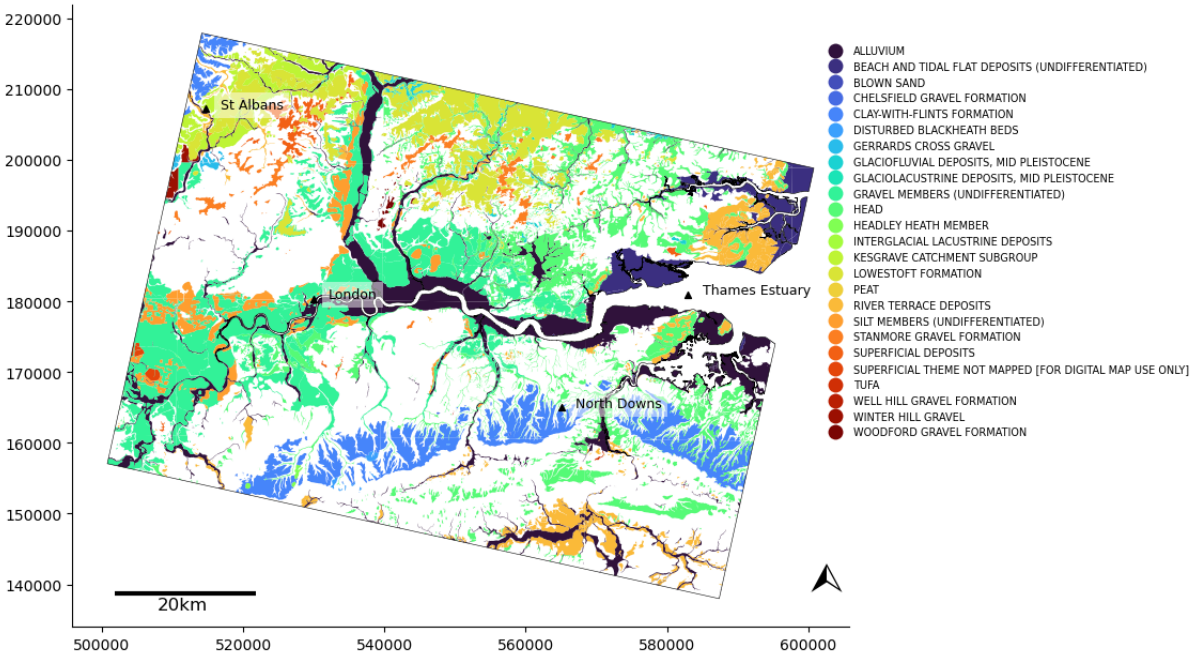

(b) Superficial

Figure 2.7: Bedrock and Superficial Geology of London Study Area

missing measurements for some years were imputed with the last known yearly average.

To approximate the continuous levels of groundwater, the borehole water level measurements were interpolated over the total bounds of the borehole data, using the ordinary kriging method. The convex hull of borehole points was used to clip the interpolated data to ensure no extrapolation of water levels was considered. The results are displayed in Figure 2.8. After this, correlations between the average ground motion velocity between 2016-2020 and groundwater levels were estimated.

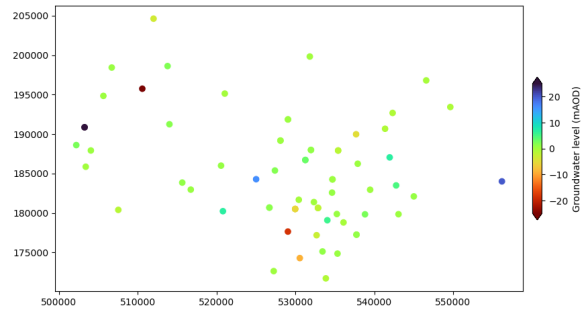

(a) Borehole water level change 2016-2020

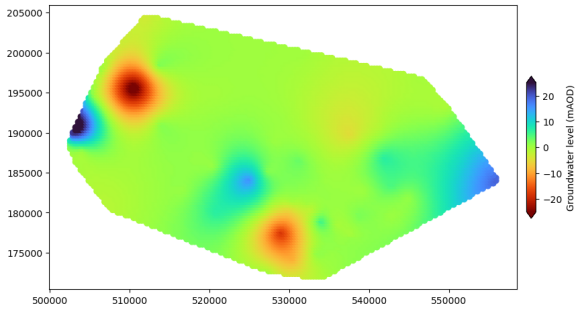

(b) Interpolated borehole values

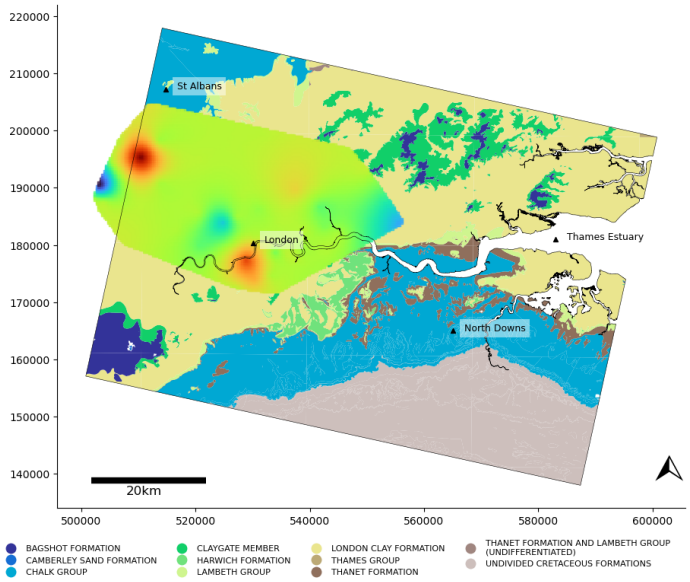

(c) Water level data in study area

Figure 2.8: Borehole measurements of water level change and interpolated values, and the locations in reference to the study area.

Chapter 3

Results

In this chapter the results of the SubCoast and EGMS comparisons are presented, displayed and discussed. Results are included for the nationwide comparison of EGMS average velocity and SubCoast PSR, as well as the case study for London, and the recalibration of PSR. For clarity, EGMS subsidence metrics will be referred to as *average velocity* and SubCoast PSR as *PSR*. All comparisons between the difference between average velocity and PSR only consider areas without uplift; i.e. polygons with an average velocity <= 0 mma^{-1}.

3.1 Comparison of Average Velocity and PSR Across Britain

Figure 3.1a shows the spatial distribution of average velocity and PSR differences across Britain. Overall, the mean difference between the two datasets is 0.56 mm with a standard deviation of 2.13 mm, and a range between -31.0 to 7.1 mm. Excluding areas with an overall PSP of 0 gives a mean difference of 0.82 mm and a standard deviation of 2.17 mm. Table 3.1 shows that 17.6% of the total area has a difference between -0.5 to +0.5 mm, and 83.3% is between ±1.5 mm. As Figure 3.1b shows, the differences aren't normally distributed and follow a multi-modal distribution with peaks around -1mm, 1.5mm, and 6mm. Separating the distribution by superficial/bedrock geology shows that, when compared to the average velocity, PSRs derived from superficial PSPs tend to over predict the subsidence rate and PSRs derived from bedrock PSPs under predict the subsidence rate.

Difference Group (mm)	No. Polygons	% Polygons	Area (km^2)	% Area
<-5	2161	0.45	224.69	0.15
[-5,-2.5)	9132	1.91	1874.54	1.22
[-2.5,-1.5)	19081	3.99	6062.83	3.94
[-1.5,-0.5)	99963	20.88	52494.18	**34.1**
[-0.5,0.5]	89103	18.61	27094.98	**17.6**
(0.5,1.5]	155149	32.41	48627.83	**31.59**
(1.5,2.5]	47424	9.91	8247.51	5.36
(2.5,5]	15217	3.18	2570.9	1.67
>5	41473	8.66	6740.62	4.38

Table 3.1: Count and area of polygons by average velocity-PSR difference group. Excluding polygons with an overall PSP of 0.

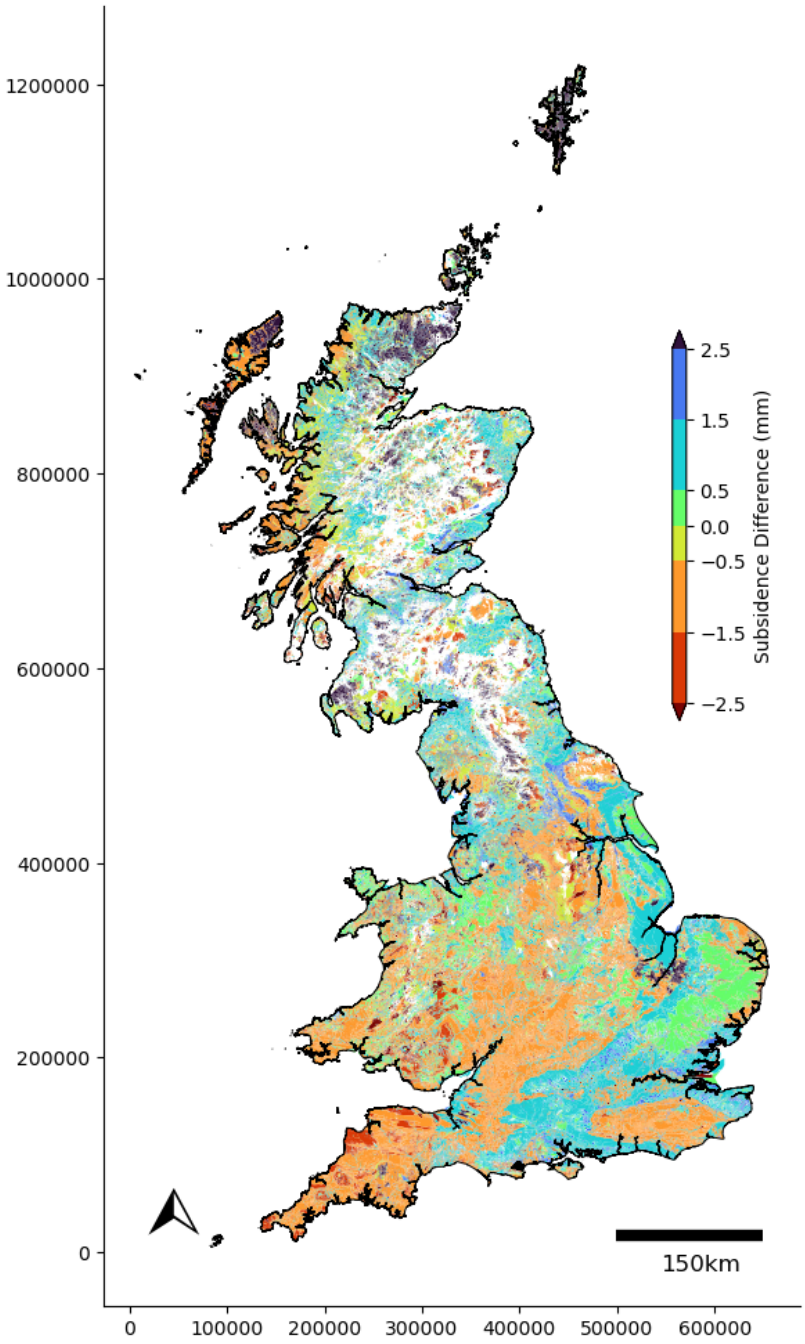

(a) Avg.velocity-PSR Map

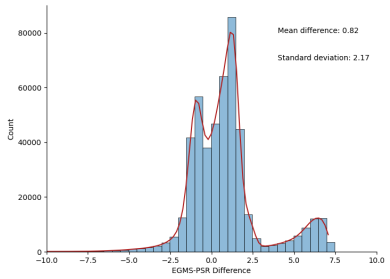

(b) Distribution of Avg.velocity-PSR

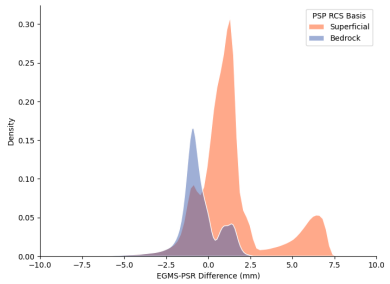

(c) Distribution of Avg.velocity-PSR by Geology type

Figure 3.1: Map of EGMS and SubCoast subsidence differences (a), the overall distribution of differences (b), and the overall differences split by bedrock/superficial geology type. The subsidence difference is calculated as average velocity - PSR, with positive differences indicating areas where the predicted PSR is subsiding faster than the measured velocity, and negative values indicate areas that are subsiding faster than predicted. The distributions are considering areas which have a PSP < 0 and average velocity <= 0 mma^{-1}.

The peak in the distribution around 6 mm is due to the subsidence difference for peat, which has a PSR of -7.06 mm compared to an average velocity of -1.34 mm. This can be seen clearly in Figure 3.2 which shows the subsidence differences and underlying geology supergroups for South East England. The large green area within 0-0.5 mm is diamicton, which accounts for 58.3% of subsiding areas within $\pm$0.5 mm of PSR in the entire dataset. Areas of peatland are clearly distinguished in red in Figure 3.2b, and show a difference > 2.5 mm in Figure 3.2c.

Overall, the spatial distribution of differences follows the geology basis that provides the overriding PSP and derived PSR values (Figure 2.3a), with areas in middle and south-west England, and areas on the west coast of Scotland subsiding between 1.5 to 0.5 mma^{-1} faster than the predicted PSR.

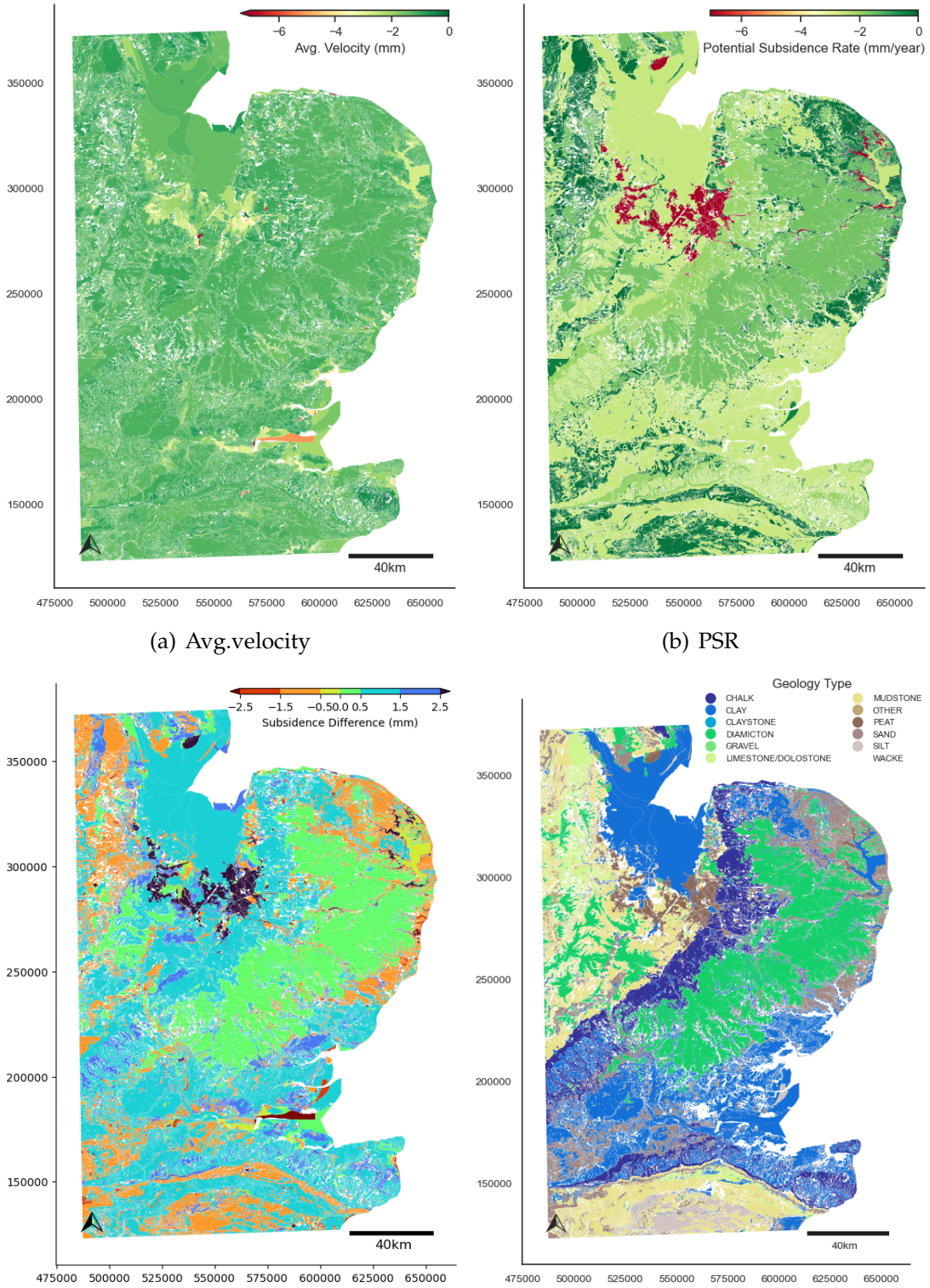

(a) Avg.velocity (b) PSR

(c) Avg.Velocity-PSR Difference (d) Geology supergroup

Figure 3.2: Maps showing the spatial distribution of average velocity (a), PSR (b), average velocity - PSR difference (c), and underlying geology type (d) in the South East of England.

3.1.1 Overall PSP

Figure 3.3 shows the distribution of the average subsidence velocity by overall PSP value. There is a clear distinction in the relationship between average velocity and overall PSP; for PSPs greater than 6, the predicted PSR is faster than the average measured subsidence velocity, whereas for PSPs less than or equal to 6 the PSR is slower. Additionally, whilst the size of the subsidence velocity is different from PSR, the trends in subsidence rate are similar for PSPs >= 19 with the velocity increasing as the PSP rises. This trend isn't visible in the velocities <= 6, which, with the exception where PSP = 5, are fairly flat.

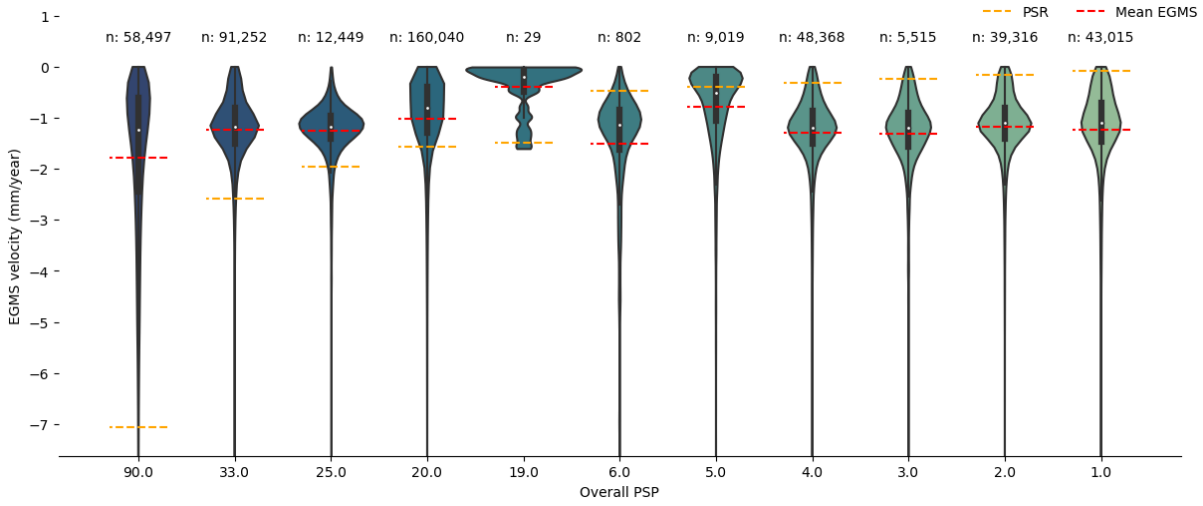

Figure 3.3: Violin plot showing the distribution of average subsidence velocity by overall PSP value. The dashed lines show the mean velocity (red) and associated PSR values (yellow) for each PSP, and the numbers above each distribution show the number of polygons with the respective PSP. The exact mean velocity values are displayed in column 'Subs μ' of Table 3.2

Table 3.2 shows the different measures of average velocity, as described in Section 2.3, compared with PSP and PSR. With the exception of PSPs 5 and 6, which are effectively 0 mma^{-1}, all other groups are subsiding on average, with an average velocity (μ) range of -0.414 to -1.337 mma^{-1} and a standard deviation between 0.656 to 1.805 mma^{-1}. Although the different velocity metrics yield variations in the values, the overall trend with PSP and PSR is similar to that displayed in Figure 3.3. Almost all PSP values have a large number of representative sample points, with the exception of 19 which only has a total of 38 polygons and 78 EGMS MPs. Therefore, the velocity statistics derived from this PSP may not be as robust as others.

PSP	PSR	No. Poly	No. MP	μ	σ	Subs μ	Wtd μ	Wtd Subs μ	Wtd $\mu - 2\sigma$
0	0.0	83984	1115309	-0.414	1.154	-0.926	-0.539	-0.79	-2.847
1	-0.079	43801	602473	-0.818	1.293	-1.224	-0.933	-1.11	-3.519
2	-0.157	39853	352789	-0.903	1.042	-1.163	-1.035	-1.158	-3.119
3	-0.236	5565	65463	-1.125	1.068	-1.318	-1.258	-1.317	-3.394
4	-0.314	48823	609189	-1.024	1.151	-1.293	-1.119	-1.24	-3.421
5	-0.393	9651	50725	0.1	1.211	-0.782	0.049	-0.651	-2.372
6	-0.472	804	12690	-1.391	1.38	-1.506	-1.059	-1.162	-3.819
19	-1.493	38	78	0.089	0.731	-0.381	-0.118	-0.496	-1.58
20	-1.572	165530	1232313	-0.547	1.247	-1.017	-0.625	-0.881	-3.118
25	-1.965	12475	150677	-1.242	0.656	-1.258	-1.171	-1.172	-2.483
33	-2.593	92389	720019	-0.969	1.071	-1.231	-1.107	-1.25	-3.25
90	-7.073	59774	516192	-1.337	1.805	-1.78	-1.154	-1.348	-4.765

Table 3.2: Comparisons between Overall PSP, PSR, mean velocity (μ), subsidence-only velocity (Subs μ), weighted mean velocity (Wtd μ), weighted subsidence velocity (Wtd Subs μ), and 2 standard deviations below the weighted mean (Wtd $\mu - 2\sigma$).

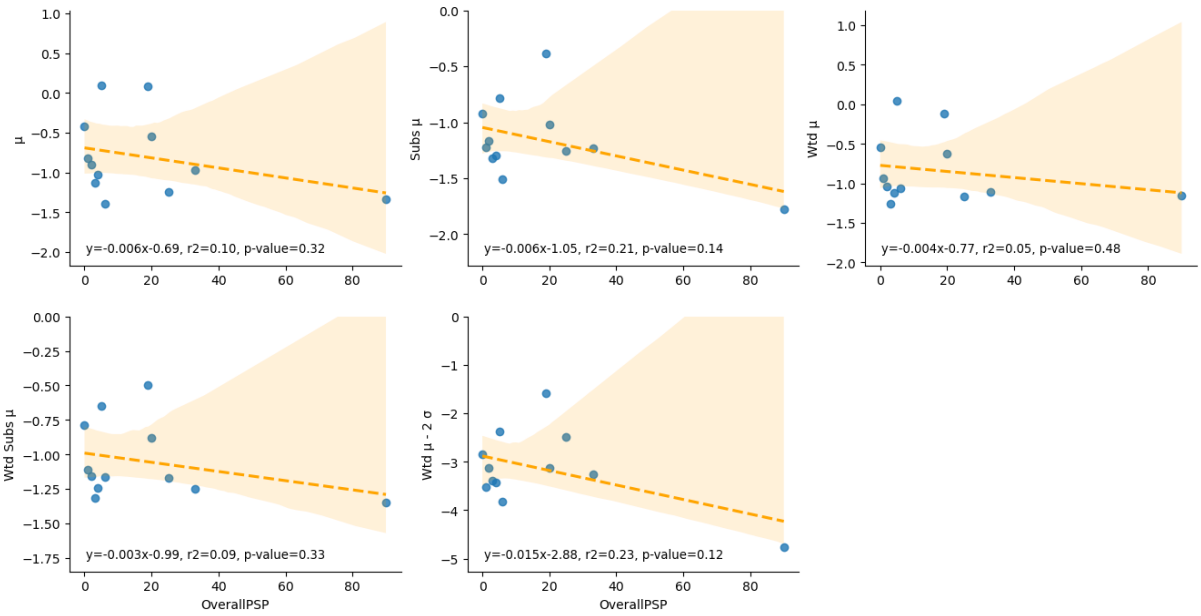

Figure 3.4: Regression plots to show the linear relationship between overall PSP and different average velocity metrics. The orange dashed line shows the regression line and the translucent orange band around this shows the 95% confidence interval.

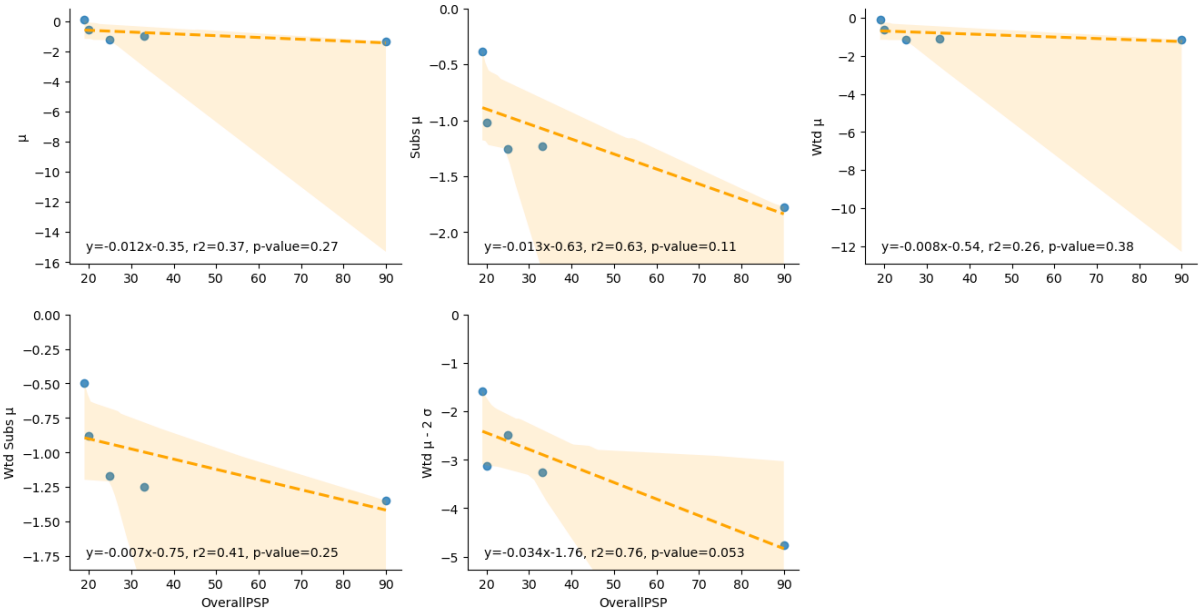

Figure 3.5: Regression plots to show the linear relationship between overall PSP and different average velocity metrics where the overall PSP is >= 19.

Across all PSP values, there isn't a significant linear relationship with any average velocity metric (see Figure 3.4). The metrics with the highest correlation are average subsidence velocity (Subs μ) and weighted mean - 2 standard deviations (Wtd $\mu - 2\sigma$), with an R^2 of 0.21 and 0.23 respectively. This is expected, as the Wtd $\mu - 2\sigma$ is inline with how SubCoast PSRs were calculated. However, this is largely due to the relative outlier at 90 PSP which has a strong influence on the linearity of the relationship. This is also evident from the confidence interval bounds, which dramatically increase with PSP. Figure 3.5 confirms the earlier observations that there is an increased linear trend with higher PSP values. Each velocity metric has improved regression statistics, with Wtd $\mu - 2\sigma$ R^2 increasing to 0.76 and a p-value of 0.053 suggesting there is a statistically significant relationship with 90% confidence.

3.1.2 Geology Supergroup

Table 3.3 shows the percentage area of each supergroup within each subsidence difference group. As presented in the previous section, there is a clear distinction between predicted and actual subsidence values where the PSP > 6 due to the difference in PSR and an overall flat average velocity distribution. There is some variation with the velocity for each PSP group, with 56% of Wacke between -0.5 to 0.5 mma^{-1} of PSR compared to an average of 8.5% for other lithologies within the PSP 1 group. While the majority of geologies are within -1.5 to -0.5 mma^{-1}, 9.1% of gravel areas are subsiding between 2.5 to 5 mma^{-1} quicker than PSR and 18.6% of sandstone areas are 1.5 to 2.5 mma^{-1} quicker.

For geologies with a PSP >= 19, the overall pattern is reversed, with most subsiding 0.5 to 1.5 mma^{-1} slower than PSR. Peat is a clear exception, where 94% of areas are subsiding > 2.5 mma^{-1} slower than predicted. However, there are also instances where the average subsidence velocity is quicker than predicted; for diamicton deposits, 1.69% of the area is subsiding -1.5 to -5 mma^{-1} quicker than PSR, and 0.66% for clay. The breakdown between each geology supergroup and the average velocity metrics and PSR can be found in Table 3.4.

Geology Supergroup	Overall PSP	<-5	[-5,-2.5)	[-2.5,-1.5)	[-1.5,-0.5)	[-0.5,0.5]	(0.5,1.5]	(1.5,2.5]	(2.5,5]	>5
GRAVEL	1.0	0.07	9.08	8.89	74.54	7.42				
DIAMICTITE	1.0		13.87	17.34	**61.31**	7.49				
LIMESTONE/ DOLOSTONE	1.0	0.09	0.91	6.22	**83.88**	8.89				
SANDSTONE	1.0	0.28	3.53	18.55	**67.51**	10.13				
WACKE	1.0	0.28	2.02	6.78	**34.53**	**56.38**				
SAND	2.0	0.2	1.5	6.59	**81.51**	10.2				
SILTSTONE	3.0	0.14	1.76	6.34	**85.37**	6.39				
MUDSTONE	4.0	0.24	1.89	4.79	**81.49**	11.59				
SILT	5.0	0.32	1.35	5.06	**26.23**	**67.05**				
CLAYSTONE	6.0	0.28	0.94	3.13	**60.06**	**35.59**				
MUD	19.0					27.15	**72.85**			
DIAMICTON	20.0	0.14	0.82	0.87	2.31	**39.09**	**53.53**	3.25		
CHALK	25.0	0.01	0.13	0.09	0.45	5.87	**92.92**	0.53		
ANHYDRITE	33.0						**100.0**			
GYPSUM	33.0		0.27	0.19			1.56	**80.79**	17.19	
SALT	33.0		0.06	0.02	0.08	0.53	**94.22**	5.09	0.01	
CLAY	33.0	0.05	0.42	0.24	0.62	5.41	**66.56**	**25.64**	1.06	
PEAT	90.0	0.01	0.05	0.06	0.29	0.59	1.19	3.6	**24.05**	**70.16**

Table 3.3: Percentage area of each geology type within each difference group - the rows sum to 100%. Geologies highlighted in pink have a small sample size.

Table 3.4 displays the same PSR and average velocity comparisons presented in Table 3.2 split by geology supergroup. With the exception of lithologies with a PSP of 1 or 33, there is a one-to-one mapping between PSP and geology supergroup. There are some variations in average velocity between different lithologies within PSP groups; for instance, the weighted subsiding velocity (Wtd Subs μ) for geologies with a PSP of 33 range between -0.575 and -1.33 mma^{-1} and between -0.699 and -1.334 mma^{-1} where PSP is equal to 1. In terms of the similarity between PSR and Wtd $\mu - 2\sigma$, both Gypsum and Salt closely match PSR with values of -2.554 mma^{-1} and -2.381 mma^{-1} respectively, compared to the predicted -2.593 mma^{-1}, although the Gypsum results aren't necessarily robust due the low number of samples. The Wtd $\mu - 2\sigma$ for clay and chalk deposits are subsiding faster than the predicted PSR, by 0.667 and 0.518

mma^{-1} respectively. For litholigies within PSP 1, there is no clear pattern between the different values; deposits such as Wacke which have a Wtd μ that is close to PSR also have a relatively large standard deviation which increases the magnitude of Wtd $\mu-2\sigma$.

Geology Supergroup	Overall PSP	Overall PSR	No. Poly	μ	σ	Subs μ	Wtd μ	Wtd Subs μ	Wtd $\mu - 2\sigma$
DIAMICTITE	1	-0.079	69	-0.358	1.534	-1.257	-0.78	-1.334	-3.848
GRAVEL	1	-0.079	928	-1.142	0.938	-1.269	-1.178	-1.222	-3.053
WACKE	1	-0.079	1611	-0.062	1.513	-1.141	-0.201	-0.699	-3.227
LIMESTONE/ DOLOSTONE	1	-0.079	10463	-0.707	1.194	-1.167	-0.897	-1.078	-3.285
SANDSTONE	1	-0.079	30730	-0.922	1.285	-1.246	-1.01	-1.143	-3.581
SAND	2	-0.157	39853	-0.903	1.042	-1.163	-1.035	-1.158	-3.119
SILTSTONE	3	-0.236	5565	-1.125	1.068	-1.318	-1.258	-1.317	-3.394
MUDSTONE	4	-0.314	48823	-1.024	1.151	-1.293	-1.119	-1.24	-3.421
SILT	5	-0.393	9651	0.1	1.211	-0.782	0.049	-0.651	-2.372
CLAYSTONE	6	-0.472	804	-1.391	1.38	-1.506	-1.059	-1.162	-3.819
MUD	19	-1.493	38	0.089	0.731	-0.381	-0.118	-0.496	-1.58
DIAMICTON	20	-1.572	165530	-0.547	1.247	-1.017	-0.625	-0.881	-3.118
CHALK	25	-1.965	12475	-1.242	0.656	-1.258	-1.171	-1.172	-2.483
ANHYDRITE	33	-2.593	2	-1.15	0.071	-1.15	-1.18	-1.18	-1.321
GYPSUM	33	-2.593	76	-0.603	1.006	-0.762	-0.541	-0.575	-2.554
SALT	33	-2.593	1097	-1.339	0.526	-1.345	-1.329	-1.33	-2.381
CLAY	33	-2.593	84670	-0.937	1.087	-1.217	-1.085	-1.239	-3.26
PEAT	90	-7.073	59774	-1.337	1.805	-1.78	-1.154	-1.348	-4.765

Table 3.4: Comparisons between Overall PSP, PSR, mean velocity (μ), subsidence-only velocity (Subs μ), weighted mean velocity (Wtd μ), weighted subsidence velocity (Wtd Subs μ), and 2 standard deviations below the weighted mean (Wtd $\mu - 2\sigma$), by geology type. Cells highlighted in pink indicate lithologies with a low sample.

Wacke, Gravel, Sandstone, Limestone, Sand, Siltstone, Mudstone, Silt, Claystone

Polygons with a PSP between 1-6 account for 36% of the total area, and have an overall average velocity of -0.816 mma^{-1} and an average subsidence velocity of -1.21 mma^{-1}, which turns to uplift further north (see Figure 3.6b). As highlighted in Table 3.3, most deposits are subsiding between -0.5 to -1.5 mma^{-1} faster than predicted PSR, with the exception of wacke and silt, and don't show correlations with PSR. Wacke and silt deposits are located primarily in the north of England and Scotland, and have a weighted subsidence velocity of -0.7 mma^{-1} and -0.65 mma^{-1} respectively. In contrast, other lithologies are either distributed in southern areas or are more dispersed throughout the whole land mass.

The gravel deposits are mainly found along the coastal areas, with some inland areas in the Chilltern Hills in Buckinghamshire, East Anglia, and South Devon. Most gravel areas with a greater rate of subsidence, between -1.5 to -5 mma^{-1} faster than PSR, are detected primarily along the coastline. One area of interest is located near the new *Sizewell C* [12] nuclear power site, which is subsiding at a rate of -3.32 mma^{-1}. This could be due to some preliminary construction work. For other groups such as Sandstone and Mudstone which cover large areas (20.7% and 42.6% of all groups within PSP 1-6 respectively) there doesn't appear to be a clear pattern or correlation between the velocities.

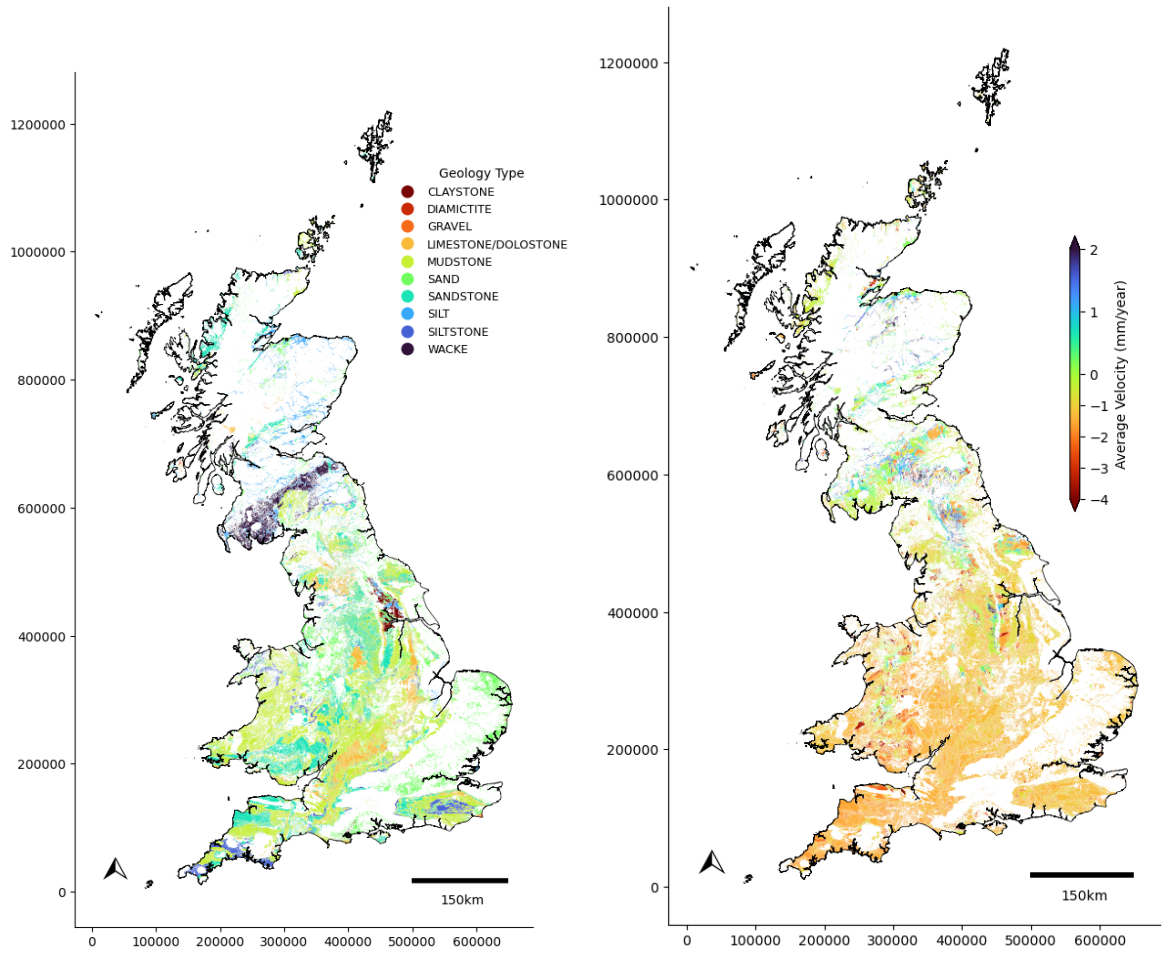

(a) Supergroup (b) Avg. velocity

Figure 3.6: Average velocity and distribution of geologies with a PSP within 1 to 6.

Peat

As described in the previous section, areas of peat are subsiding much slower compared to PSR and the relative estimates of other deposits. Figure 3.7 shows the spatial distribution of peatland in Britain, and the average velocity for 2016 and 2021. The majority of the peatland in the UK is found in Scotland, which contains 66% of the total 3 billion hectares of peatland in the UK [15], with other large areas in North England, Wales, East Anglia and Devon. Although overall from 2016-2021 the difference between PSR and average velocity is large, this varies for each year. Notably, 2016 and 2021 have very different average velocities of -0.86 and -2.44 mma^{-1} and standard deviations of 2.96 and 4.17 mma^{-1} respectively. This suggests that the increase in subsidence rate isn't uniform across all areas, which is visible in Figure 3.7c which shows the difference in average velocity between 2021 and 2016. Most peat areas in North Scotland and East Anglia are subsiding at a similar rate (shown as green), whereas areas in North England and South West Scotland have seen an increase in the rate of subsidence (shown as red). Although some of the difference in the average velocity between 2016 and 2021 can be attributed to some EGMS MPs missing in the tip of Scotland and the Orkney and Shetland islands in 2016, the 2021 velocity is still subsiding 1 mma^{-1} faster than the average velocity between 2017 to 2020 (see Figure 3.8).

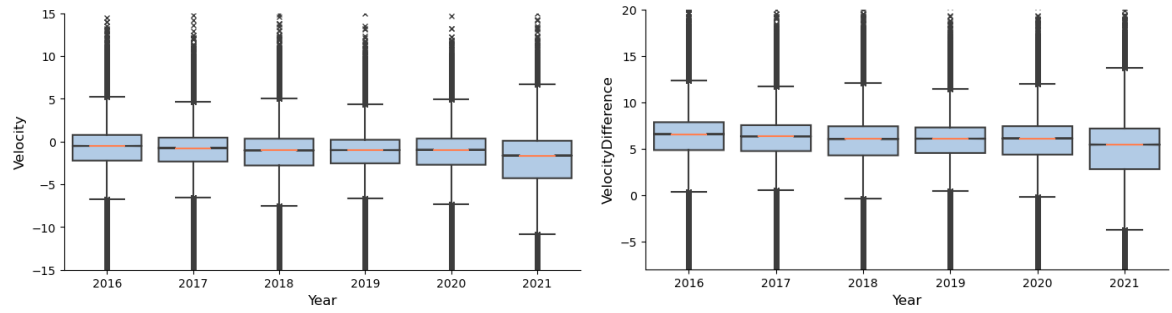

(a) Avg. velocity (b) Avg. velocity - PSR

Figure 3.8: Average velocity for peatland areas by year and the differences with PSR. With the exception of 2016, most years have a similar average value and spread, however in 2021 the average velocity is much faster and the interquartile range is more spread.

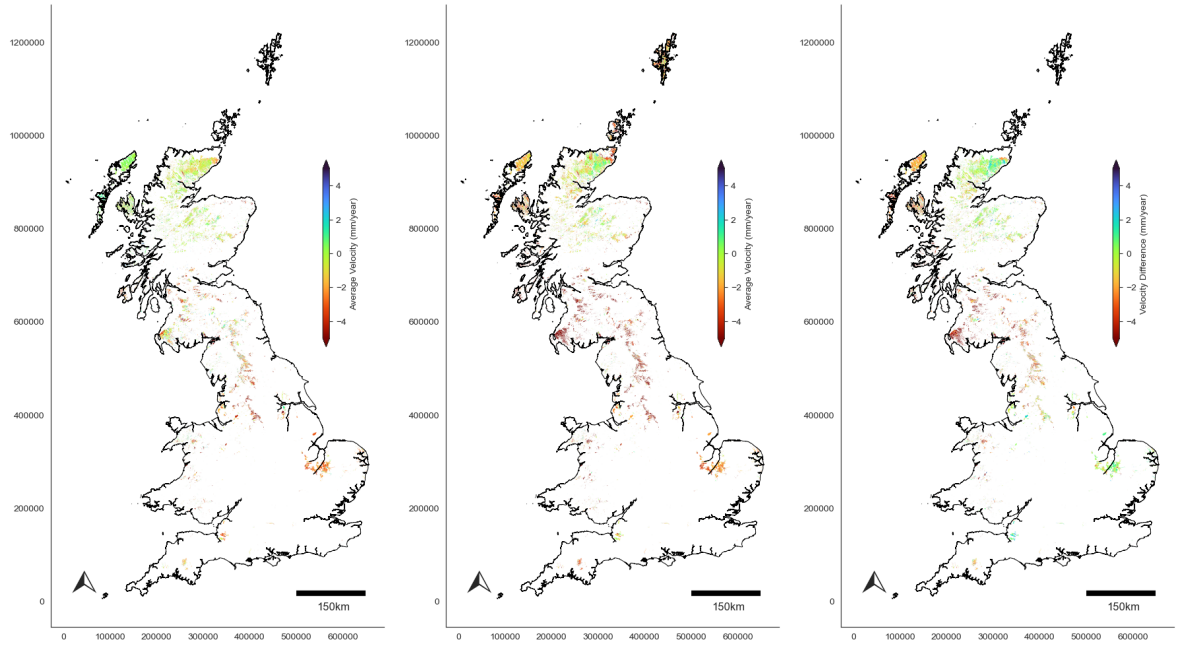

(a) (b) (c)

Figure 3.7: Average velocity for peat deposits in a) 2016, b) 2021, and c) the differences. The average velocity and differences have been limited to ±5 mma^{-1} to avoid the visualisation effects of extreme values on the colour map.

As peatland is vulnerable to subsidence from both compaction and shrinkage, there could be multiple reasons why the subsidence rate has increased in 2021. Due to the relatively large areas of sustained differences, the effects could be due to regional weather variations. Tests were run to measure the correlation between the average velocity and rainfall and temperature for 2016 - 2021, although only weak/negligible correlations were observed.

Diamicton

58.6% of all areas that are within ±5 mma^{-1} of PSR are diamicton deposits. Diamicton is also the most common type of deposit in the dataset, which accounts for 26.6% of the total area where PSP > 0. As detailed in Table 3.3, almost 40% of the diamicton areas are within ±0.5 mma^{-1} of PSR (the largest proportion of any lithology >= 19 PSP), and 53% is subsiding +0.5 to 1.5 mma^{-1} slower than PSR. From Figure 3.9 it is clear that, as identified elsewhere, the main pattern of variation with the average velocity is in the

north-south direction, with more areas subsiding slower than predicted.

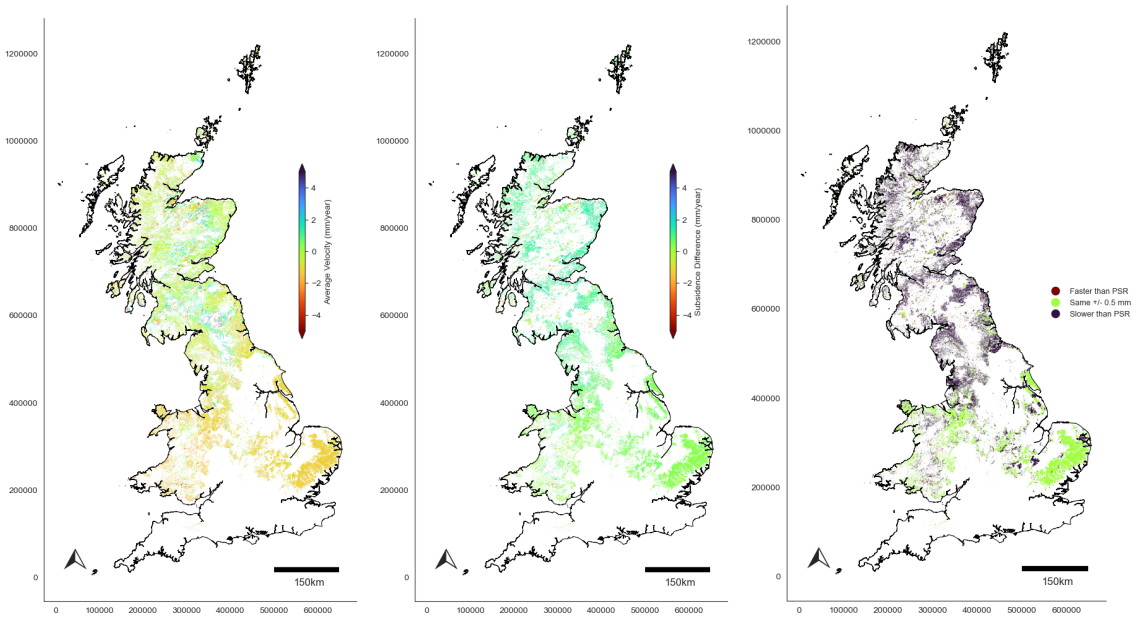

(a) Avg. velocity (b) Avg. velocity - PSR (c) Classified

Figure 3.9

Mining Hazards

The correlation between areas of mining hazard and average velocity were tested to see if the areas within these regions were moving differently to areas without such hazards. No clear correlations were found; the results are included in Appendix A.2.

3.2 Recalibration of PSR

Following the same methodology set out in the initial BGS paper [42], PSRs were re-calibrated using all the available EGMS data. Due to the lack of correlation between the average velocity and deposits with a low PSP %, the regression was only fit with the average velocity values for PSPs >= 5%; this is also somewhat consistent with how the PSRs were extrapolated in the original study, which excluded PSPs between 0 and 5% due to inconsistencies thought to be due to differences in the scale of data inputs. Table 3.5 shows the comparison between the original and re-calibrated PSRs.

The coefficient for the recalibrated model is 16% weaker than the orginal SubCoast model, which indicates that the relationship between PSP and average velocity isn't as strong as in the original study. Furthermore, by fitting the regression without an intercept, the overall fit has reduced significantly, and the R^2 is now negative at -0.84 (down from 0.76 with the intercept), which means that the model is worse at predicting the velocity than using a simple average.

PSP %	PSR (mma^{-1})		Difference (mma^{-1})
	Original	Recalibrated	
0	0	0	0
1	-0.079	-0.066	0.014
2	-0.157	-0.131	0.026
3	-0.236	-0.196	0.040
4	-0.314	-0.261	0.053
5	-0.393	-0.327	0.066
6	-0.471	-0.392	0.079
8	-0.628	-0.522	0.106
11	-0.864	-0.718	0.146
13	-1.021	-0.849	0.172
17	-1.335	-1.110	0.225
19	-1.492	-1.241	0.251
20	-1.570	-1.306	0.264
22	-1.727	-1.437	0.290
25	-1.963	-1.633	0.330
33	-2.591	-2.155	0.436
47	-3.690	-3.069	0.621
50	-3.925	-3.265	0.660
60	-4.710	-3.918	0.792
67	-5.260	-4.375	0.885
70	-5.495	-4.571	0.924
90	-7.065	-5.877	1.188
100	-7.850	-6.530	1.320

Table 3.5: Recalibrated and original PSR values by PSP%.

3.3 London Case Study

Figure 3.10 displays the distribution of PSR, average velocity, subsidence difference, and geology supergroups across the study area. The average velocity ranges between -48.4 to 9.4 mma^{-1} with an average of -1.25 mma^{-1} and a standard deviation of 0.68 mma^{-1}. As shown in Figure 3.10b, there are multiple regions along the Thames estuary and within alluvium deposits that are experiencing high rates of subsidence (shown in red), as well as areas of uplift north of the Thames and around Canning Town and Barking. The average difference between PSR and average velocity is 0.70 mma^{-1}, with a median of 1.19 mma^{-1} and standard deviation of 1.17 mma^{-1}. As shown in Table 3.6, 9.9% of the area is within $\pm$0.5 mma^{-1} and 90.4% are within $\pm$1.5 mma^{-1}. The distribution of differences is different to the national-level comparisons, where a greater proportion of areas were within $\pm$0.5 mma^{-1} or -1.5 to -0.5 mma^{-1} and fewer were between 0.5 to 1.5 mma^{-1} difference. This is due to the difference in relative quantities of PSPs derived from bedrock or superficial deposits between the national-level and London-level data, where 52% of the area is categorised with a geology supergroup of Clay and 18% is Chalk.

Difference Group (mm)	No. Polygons	% Polygons	Area (km^2)	% Area
<-5	13	0.08	4.23	0.06
[-5,-2.5)	61	0.39	5.65	0.08
[-2.5,-1.5)	295	1.89	55.36	0.81
[-1.5,-0.5)	2491	15.99	1669.43	**24.52**
[-0.5,0.5]	1025	6.58	676.28	9.93
(0.5,1.5]	7977	51.21	3811.36	**55.99**
(1.5,2.5]	3683	23.64	580.56	8.53
(2.5,5]	29	0.19	4.1	0.06
>5	3	0.02	0.08	0.0

Table 3.6: Count and area of polygons by average velocity-PSR difference group for the Greater London study area. Excluding polygons with an overall PSP of 0.

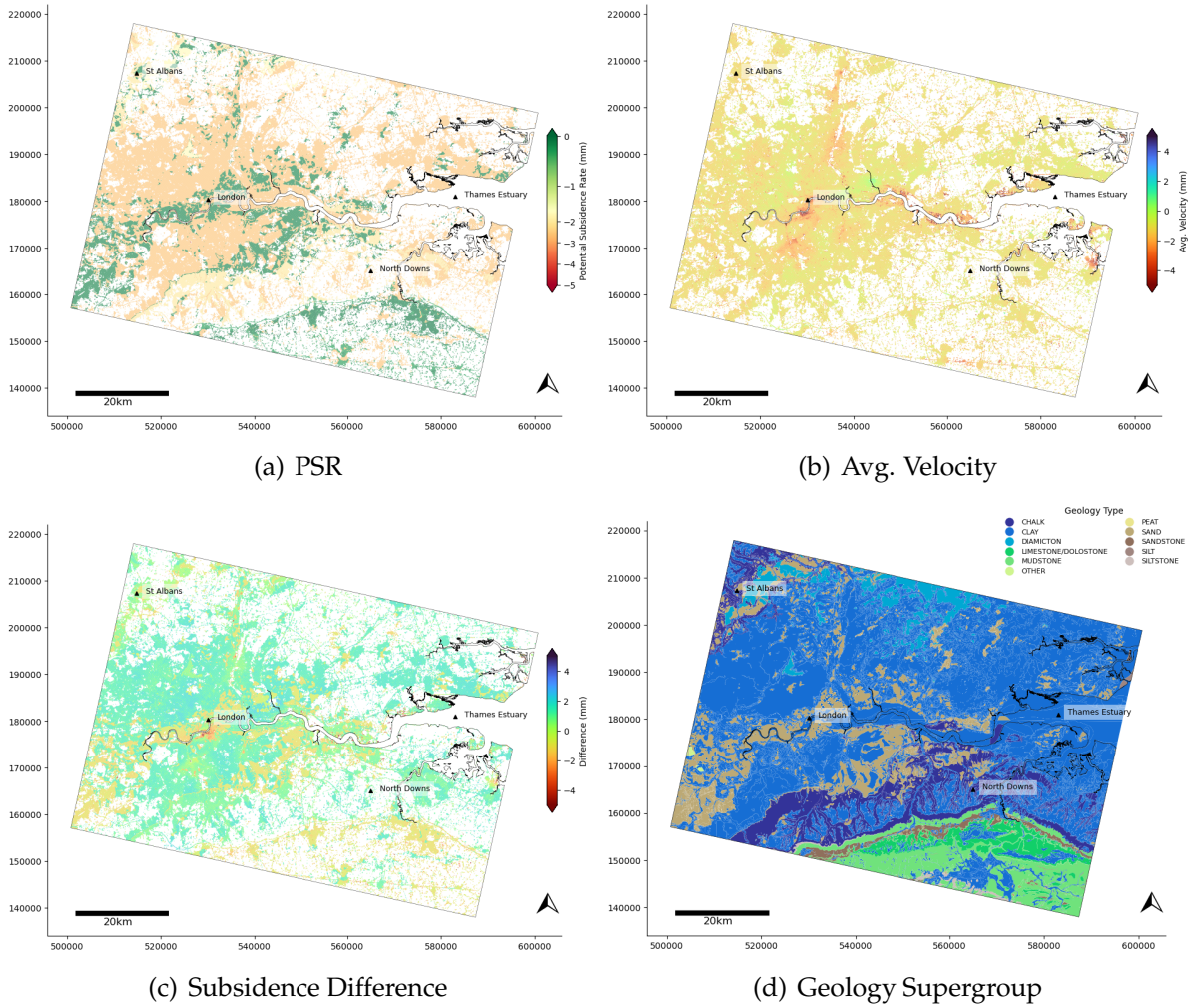

(a) PSR (b) Avg. Velocity

(c) Subsidence Difference (d) Geology Supergroup

Figure 3.10: Maps over the London study area displaying PSR, average velocity, differences, and geology types. Average velocity (b) considers all velocities whereas the subsidence difference (c) only considers areas with an average velocity <= 0 mma^{-1} and a PSP < 0.

3.3.1 Geology

Table 3.7 shows the differences between PSR and average velocity for the Greater London area. The patterns reflect the same as for the national-level comparison; lithologies with a PSP <= 6 are subsiding faster than PSR and PSPs > 6 are subsiding slower. There are some slight differences, for instance 86.8% of silt areas are subsiding between -2.5 and -1.5 mma^{-1} faster than predicted PSR, and almost 6% are subsiding

faster than -5 mma^{-1} faster. The total area for these groups is just 20 km^2, less than 1% of the total study area, and are situated in the east, near the Thames estuary. With the exception of sand, the other litholigies within 1-6 are located in the south, away from the Thames at the beginning of the north downs.

96% of diamicton is within ±0.5 mma^{-1}, whereas 97.9% of chalk and 76.3% of clay are within +0.5 to 1.5 mma^{-1}. 1.21% of clay lithologies are subsiding more than -0.5 mma^{-1} faster than PSR, and are primarily located in the alluvium and tidal flat deposits in the east towards the Thames estuary. Unlike the national-level comparisons, there isn't a clear trend with the average velocities and overall PSP.

The average velocities for each geology supergroup are included in Table 3.8, and displayed graphically in Figure 3.11. The weighted mean velocity is between -1.168 and -2.543 mma^{-1}, with silt having the fastest subsidence rate. This seams to be an artefact of having few EGMS MPs within the SubCoast polygons to derive the average velocity; this is evident when looking at the distribution in Figure 3.11. Otherwise, all average velocities (excluding peat) are very similar and vary between -1.168 and -1.28 mma^{-1}. Clay deposits have the widest range, and vary between -22.8 and 6.9 mma^{-1}, which is likely due to the shrink-swell behaviour of the London Clay. Looking at the derived statistic, the derived subsidence statistics for clay and chalk are very close to the PSR and are within 0.046 and 0.126 mma^{-1} respectively. There are no other obvious patterns between the other geology groups.

Geology Supergroup	Overall PSP	<-5	[-5,-2.5)	[-2.5,-1.5)	[-1.5,-0.5)	[-0.5,0.5]	(0.5,1.5]	(1.5,2.5]	(2.5,5]	>5
LIMESTONE/ DOLOSTONE	1.0		0.03	1.69	**98.24**	0.04				
SANDSTONE	1.0		0.08	1.72	**97.91**	0.29				
SAND	2.0		0.43	3.8	**94.83**	0.93				
SILTSTONE	3.0		0.35	1.36	**97.8**	0.49				
MUDSTONE	4.0		0.03	0.35	**99.33**	0.29				
SILT	5.0	5.89		**86.78**	7.33					
DIAMICTON	20.0		0.02	0.05	0.05	**96.39**	3.48			
CHALK	25.0			0.01	0.07	2.0	**97.9**	0.02		
CLAY	33.0	0.09	0.06	0.11	0.95	4.55	**76.36**	17.77	0.12	
PEAT	90.0								27.27	**72.73**

Table 3.7: Subsidence differences for each geology group in London.

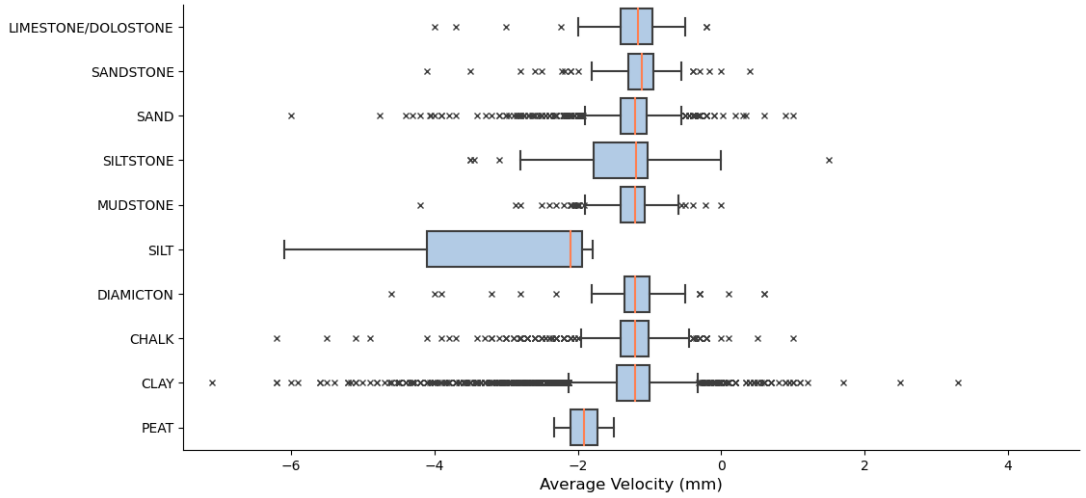

Figure 3.11: Distribution of average velocity by Geology Supergroup

Geology Supergroup	Overall PSP	Overall PSR	Area (km^2	Min	Max	Median	Wtd μ	σ	Wtd Subs μ	Wtd $\mu - 2\sigma$
LIMESTONE/ DOLOSTONE	1	-0.079	158.886	-4.0	-0.2	-1.162	-1.197	0.576	-1.197	-2.349
SANDSTONE	1	-0.079	74.62	-4.1	0.4	-1.11	-1.166	0.508	-1.167	-2.182
SAND	2	-0.157	685.87	-6.0	1.0	-1.2	-1.223	0.443	-1.226	-2.108
SILTSTONE	3	-0.236	77.356	-3.5	1.5	-1.183	-1.174	0.904	-1.175	-2.982
MUDSTONE	4	-0.314	685.075	-4.2	0.0	-1.2	-1.282	0.39	-1.282	-2.062
SILT	5	-0.393	20.866	-6.097	-1.79	-2.101	-2.543	2.402	-2.543	-7.347
DIAMICTON	20	-1.572	510.627	-4.6	0.6	-1.195	-1.231	0.57	-1.232	-2.372
CHALK	25	-1.965	1327.379	-6.2	1.0	-1.2	-1.168	0.462	-1.168	-2.091
CLAY	33	-2.593	3266.265	-22.778	6.9	-1.2	-1.275	0.636	-1.277	-2.547
PEAT	90	-7.073	0.112	-2.333	-1.5	-1.908	-2.017	0.352	-2.017	-2.72

Table 3.8: Average velocities for geology supergroups in London.

London Thames Area

Within the whole London study area, no clear patterns were found between the bedrock geology and average velocity, with the median average velocity consistent for all groups ranging between -1.3 to -1.1 mma^{-1}, and the mean velocity between -1.12 and -1.38 mma^{-1}. With the superficial geology, as noted earlier, significant areas of subsidence are located within the alluvium and tidal deposits. This can be seen more clearly in Figure 3.12, which shows the distribution of average velocity along the Thames in greater detail. Figure 3.12c shows multiple areas near the banks of the Thames that are subsiding at a rate < -4 mma^{-1}, with large areas of red (denoting subsidence) south of the City of Westminster near Battersea, and west of the City of London. Towards the east, there are patches of fast moving subsidence however the majority of these are within the range of natural subsidence motion for clay litholigies (-2.593 mma^{-1}). This is displayed clearly in Figure 3.12d, where the subsidence difference is largely centered around 0 mma^{-1} (shown as green) with a few areas of faster moving subsidence in red. The large orange areas of difference are due to differences between the measured velocity and PSR for sand lithologies (see Figure 3.12b) which have a PSR of -0.157 mma^{-1}. As mentioned previously, there are areas of uplift on the north of the Thames, which are especially prevalent around Barking.

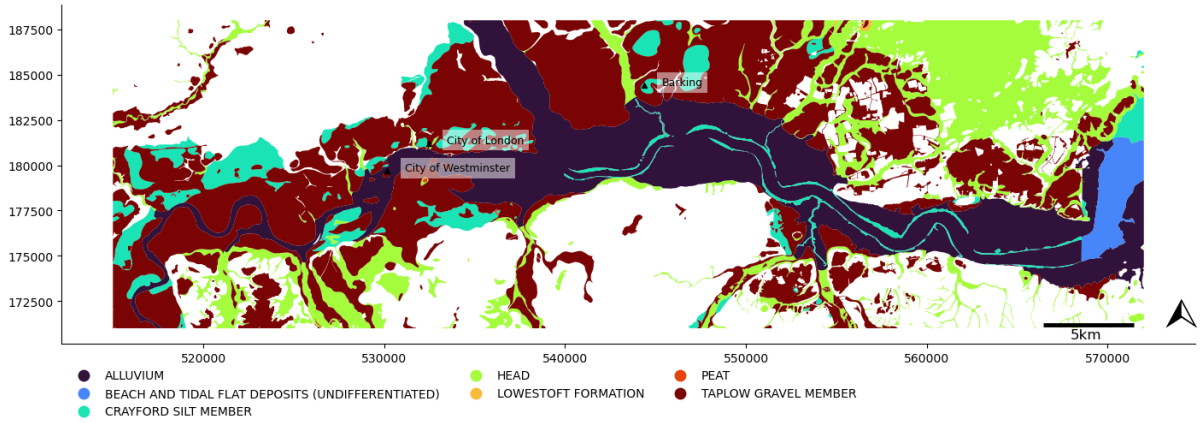

(a) Superficial geology

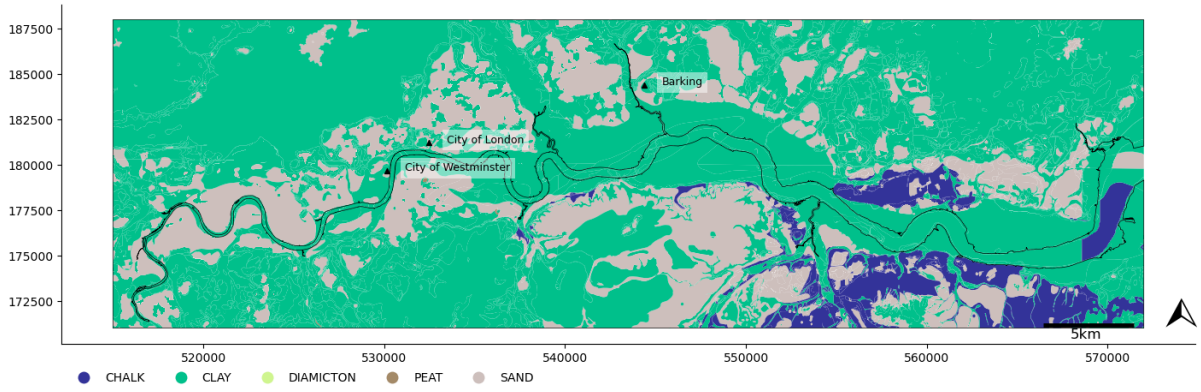

(b) Geology supergroup

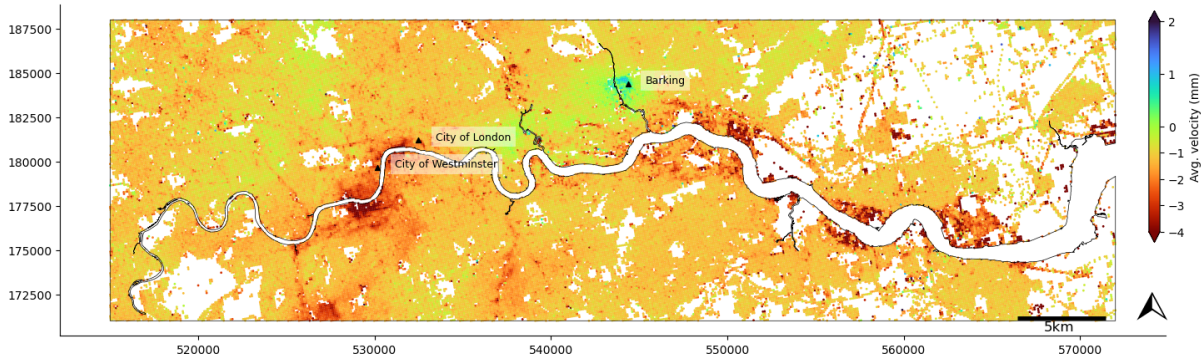

(c) Average velocity

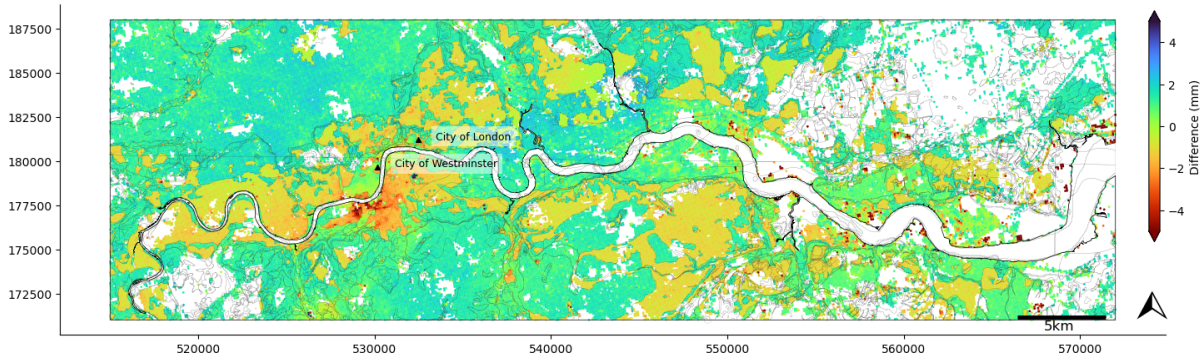

(d) PSR subsidence differences

Figure 3.12: Maps of the Thames river showing the different types of geology and velocity measurements. The lines on the subsidence difference map (d) are the individual polygon boundaries denoting the geology supergroups in (b).

3.3.2 London Underground Work

The London underground is the largest metro network in Europe [11], with a total length of 402 km transporting an average of 1.35 billion passengers annually [49]. To maintain the proper working of the service, regular updates and maintenance are carried out on the network, in addition to extending old lines to connect new stations and creating entirely new sections of tunnels. Recent large scale projects have included Crossrail/Elizabeth Line, which created 42 km of new rail tunnels under London from Royal Oak Portal to Farringdon between May 2012 and May 2015 [14], and other smaller extensions to the overground network and construction of a new station, Barking Riverside, between 2018 - 2022.

Northern Line Extension

The largest underground construction project during the 2016 - 2021 time frame, was the Northern Line extension connecting Kennington to two new tube stations at Battersea Power Station, on Battersea Park Road, and Nine Elms on Wandsworth Road. The Major construction construction work commenced in November 2015, with two tunnel boring machines creating a new 3km section of tunnel between Battersea and Kennington from March - November 2017, and further tunneling work carried out for new customer passageways at Kennington Tube station in 2018 [2].

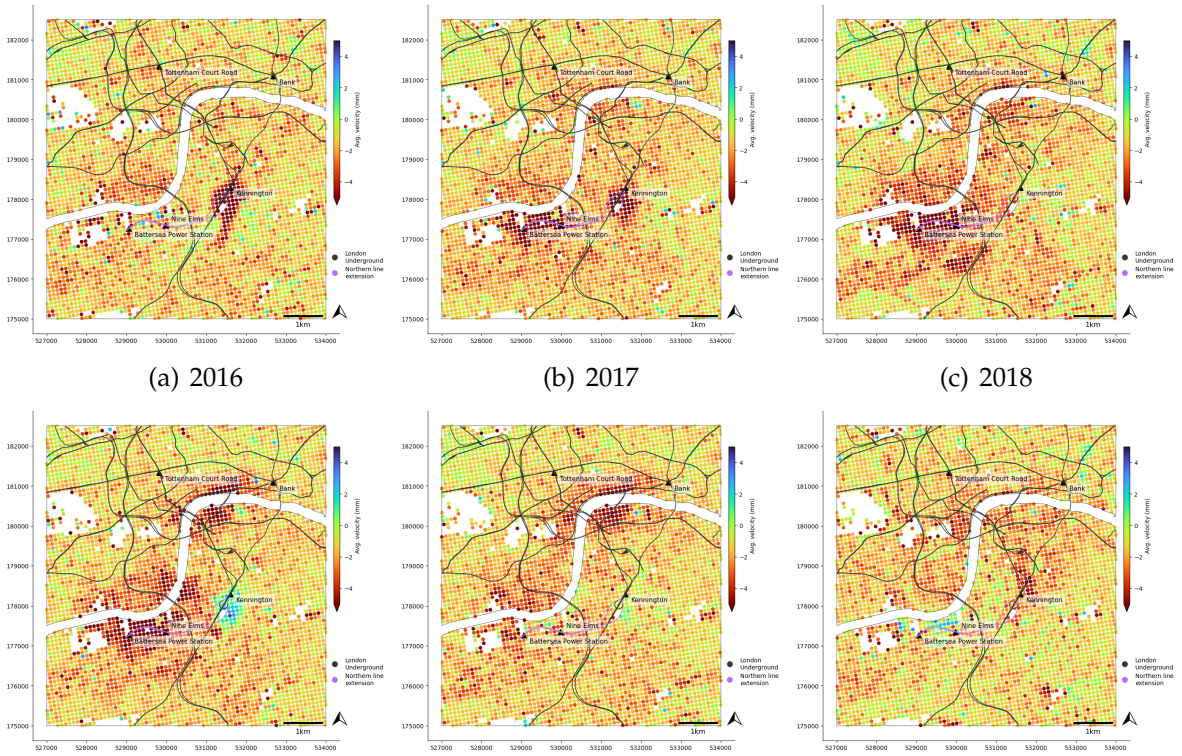

(a) 2016 (b) 2017 (c) 2018

(d) 2019 (e) 2020 (f) 2021

Figure 3.13: Ground motion maps around Battersea Park underground station and Kennington for 2016 to 2021. An extension to the Northern Line network connecting Kennington and Battersea Park was built between 2016 to 2018.

From 2016 - 2021, the average velocity in a 500 m radius around Battersea Power Station, Nine Elms, and Kennington was -4.44, -3.93, and -1.73 mma^{-1} respectively, against an average velocity of -1.27 mma^{-1} for the 412 other stations. Figure 3.13 shows the

spatial distribution of average velocity for each year between 2016 and 2021. As can be seen, there are distinct areas of subsidence around each station during the main construction dates, with maximum yearly subsidence levels of -5.6 mma^{-1} for Battersea Power Station in 2018, -5.23 mma^{-1} for Nine Elms in 2018, and -4.84 mma^{-1} for Kennington in 2016. There is an area of uplift surrounding Kennington station in 2019 which contributes to a relatively slow subsidence rate for the entire 2016 - 2021 period.

3.3.3 Groundwater Abstraction

As mentioned in Section 1.1.5, changes in groundwater level are a major cause of ground motion, and abstraction of groundwater from subsurface aquifers can have a regional-level impact on the height of the ground surface. The principal aquifers in London are the Chalk Group, Oolitic Limestones, and the cross-bedded sand and fine-grained sands and sandstones of the Lower Greensand Formation [1]. Groundwater levels in London have been closely monitored and controlled since the development of the General Aquifer Research Development and Investigation Team (GARDIT) strategy in 1992, which was a response to the threat posed to structures following significant ground level changes due to the over-exploitation of aquifers in the 1960s and the subsequent uplift from groundwater rebound following the cessation of industrial activities [19].

Groundwater levels were obtained for 59 boreholes in the London study area, with a varying number of observations for each borehole for each year; the average number of measurements per borehole for 2016 was 7.45, 9.73 in 2017, 48.7 in 2018, 20.4 in 2019, and 4.4 in 2020. Figure 3.15b shows the interpolated groundwater differences between 2016 and 2020. Visually, there are similarities between areas of subsidence and groundwater withdrawal. Particularly around the Battersea area, there is a large area of ground withdrawal that aligns with the subsidence pattern, as well as areas of rebound and uplift near Barking, and a wide area pattern of slow moving subsidence west of Chigwell that also aligns with groundwater withdrawal.

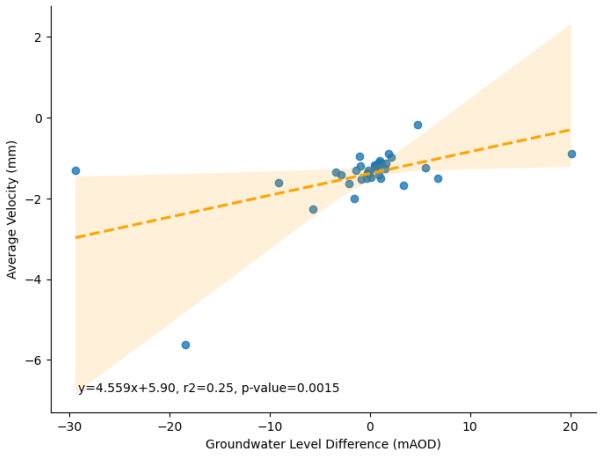

Figure 3.14: Caption

Overall, the correlation between the interpolated groundwater level data and the average velocity is only weak, with a Pearson correlation coefficient of 0.26 and a Spearman correlation of 0.32. This is likely due to the sparsity of the boreholes, especially further

away from the London city region, and where boreholes were missing data values for certain years. To account for these potential sources of error, a simpler test was run to just consider the EGMS MPs that were within 250 m of the boreholes. Boreholes missing measurements for 2016 or 2021 were dropped from the dataset, which resulted in a total of 38 boreholes with adequate data. The correlation between average velocity and groundwater change for these points increased to 0.50 and 0.53 for Pearson and Spearman correlation respectively, with a p-value < 0.01. The relationship between these variables is included in Figure 3.14.

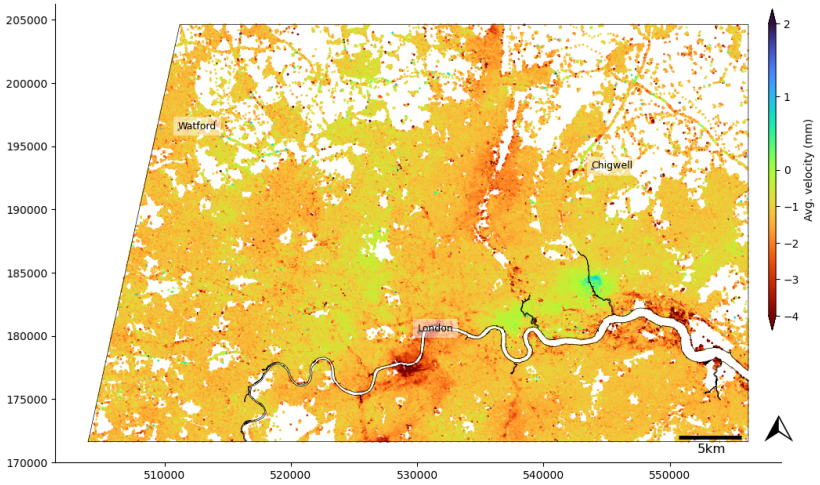

(a) Average Velocity

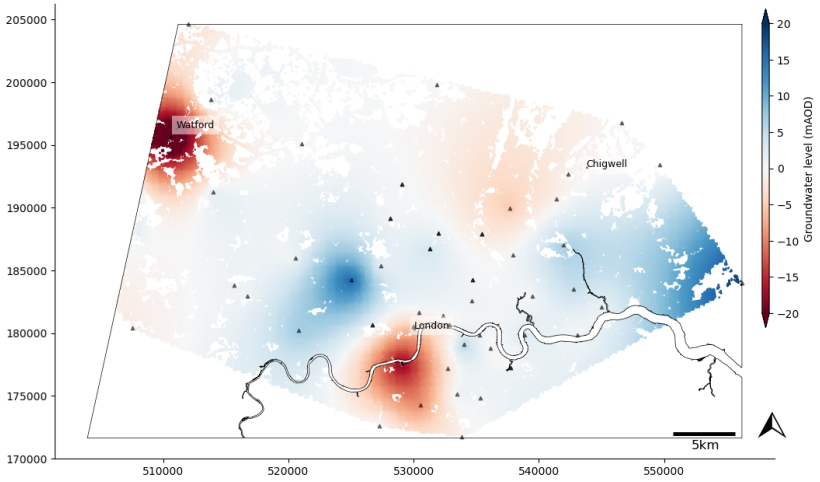

(b) Groundwater level change (2016 - 2020)

Figure 3.15

Chapter 4

Discussion

In this chapter, the analysis results presented in the previous chapter are discussed in further detail. The results are contextualised with findings in similar studies and possible causal factors are introduced which may explain some of the particular outcomes. This is done for both the national-level and London-level case study.

4.1 National-level Subsidence

As presented in Section3.1.1, there is weak/negligible correlation between PSR and average velocity, with an overall Pearson correlation of 0.18 and Spearman correlation 0.07 for subsiding areas, and an R^2 of 0.21 when just considering the mean values for each PSP (with a p-value of 0.14 suggesting that the relationship isn't significant). Although the overall correlation is negligible, there is a linear trend when considering the areas with a PSP >= 19%. This linearity is enhanced by peat and mud, which have much faster/slower average subsidence velocities, -1.78 and -0.38 mma^{-1} respectively, when compared to the other lithologies with a PSP of 33%. For all lithologies >= 19% PSP, the average subsidence velocity is much slower than the predicted PSR; this is to be expected, as PSR is a measure of the maximum natural annual subsidence rate, so this should only be surpassed, in theory, due to increased subsidence from human activities. The derived subsidence statistics (Wtd $\mu - 2\sigma$) are much closer to the predicted PSR, with an average absolute difference of 1.02 mma^{-1} ranging between -0.087 to 2.31 mma^{-1}.

For the other lithologies <= 6% PSP, the opposite behaviour was observed; all average velocities were much lower than the predicted PSR values, with an average difference of 0.94 mma^{-1} for the average subsidence velocity and -3 mma^{-1} for the derived subsidence statistic. Given that the predicted PSRs for these groups are effectively 0 mma^{-1} (range between -0.079 to -0.472 mma^{-1}), it is expected that many areas will be subsiding at a faster rate. Differences on this scale could also be due to inherent uncertainties in the InSAR measurements. However, the magnitude of subsidence for these groups is the same as for PSPs between 19 and 90%, which are more susceptible to subsidence due to shrinkage, compaction, and dissolution, which suggests that there are some other unconsidered factors that are effecting the ground-level change.

For mining areas, there were no significant differences found between the mining category hazard group and average velocity. There are a couple of reasons for this; firstly,

the mining dataset excluded coal mining areas, and secondly there was no indication as to how recent the mining activity had been undertaken. Without this information there is little reason for there to be a relationship between the variables, as the described activity could have taken place years before the InSAR data begins.

4.1.1 Wide-area displacements

Although there was no strong correlation between PSR and average velocity on a national-level, there were some clear spatial trends in the average velocity; principally, an increase in uplift in northern England and Scotland, and subsidence in the south. By crudely splitting the landmass by administrative boundaries, the combined average velocities for England and Wales was -1.17 mma^{-1}, compared to -0.48 mma^{-1} in Scotland (including Orkney and Shetland Islands). This trend is shown more clearly in Figure 4.1, which shows the average velocity against northings. For slow moving 'stable' MPs (average velocity within $\mu \pm 2\sigma$) there is a moderate/strong correlation with northings, with a Spearman ρ of 0.68 and an average increase in the velocity of approximately 0.08 mm for every 100 km increase in northings.

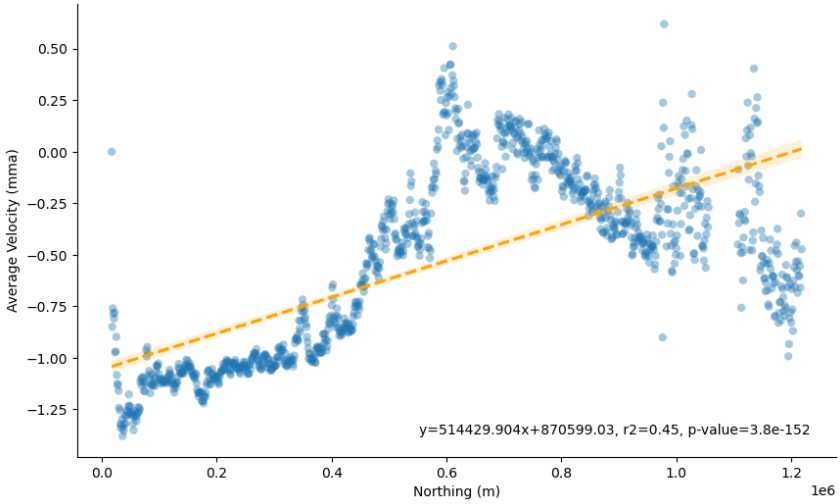

Figure 4.1: Scatterplot showing the average velocity for every 1000 m against northings. The average velocity considered here are just the 'stable' points, excluding any measurements that are greater/less than $\mu \pm 2\sigma$.

Geology Supergroup	Scotland	England	Wales
ANHYDRITE		-1.18	
CHALK		-1.192	
CLAY	-0.703	-1.306	-1.518
CLAYSTONE	-1.179	-1.202	
DIAMICTITE	-1.51		
DIAMICTON	-0.973	-1.053	-1.345
GRAVEL	-1.015	-1.267	-1.558
GYPSUM		-0.638	
LIMESTONE/DOLOSTONE	-0.93	-1.129	-1.385
MUD	-0.498	-1.321	
MUDSTONE	-1.518	-1.314	-1.44
PEAT	-1.388	-3.244	-2.221
SALT		-1.342	-0.833
SAND	-0.83	-1.214	-1.359
SANDSTONE	-0.831	-1.362	-1.442
SILT	-0.712	-1.154	-1.138
SILTSTONE	-1.272	-1.376	-1.372
WACKE	-1.419	-1.054	

Table 4.1: The average velocities (mma^{-1}) for each geology supergroup, split by country.

Although the differences in the average ground displacement could in theory be due to the make-up of the underlying geology and distribution of lithologies, Table 4.1 shows that, with the exception of wacke and mudstone, the average velocities for all geology groups are subsiding slower than in either England or Wales, which suggests that the cause of the velocity change isn't due to the geology type. The large-scale trend in the ground-level displacement indicates that the source of the displacement is much larger than what would be typical from the local geology types.

One such explanation for the observed motion could be due to Postglacial Isostatic Adjustments (PIA) resulting from the deglaciation of the British–Irish ice sheet and the adjacent Fennoscandian ice sheet; this process has been found to effect the vertical component of large-scale ground motions, and resulted in subsidence on the Shetland Islands, uplift in many areas of Scotland, and subsidence in large parts of England and Wales [50]. Many studies have been conducted to model the vertical component of motion and utilised various approaches, including combinations of lithosphere thickness models, historic sea level rise data, absolute gravity measurements, and continuous GNSS station observations. Time-series of continuous GNSS station measurements give an average velocity of 0.38 mma^{-1} ($\pm$0.42 mm) for Scotland (0.21 mma^{-1} $\pm$0.44 mm including Shetland), and -0.74 mma^{-1} ($\pm$0.5 mm) for England and Wales [27]. These measurements are inline with the observations from the EGMS InSAR data, with England & Wales average velocity -1.17 mma^{-1} within the lower bound of -1.24 mma^{-1} of the GNSS measurements, and Scotland and Shetland EGMS measurements -0.25 mm away from the GNSS lower bound. The differences between the two datasets could be attributed to the increased spatial resolution of the InSAR data compared with the sparsity of the GNSS network. The similarity between the areas and scale of uplift and subsidence suggest that the large-scale trend in the InSAR data is due to PIA. Furthermore, these wide-area ground motions would be present in the EGMS data as the Calibrated and Ortho product utilise a GNSS model to fix the InSAR measurements to a common reference frame [35], but wouldn't be included in the InSAR measurements used to calibrate the PSR values in the original SubCoast calculations due to the smaller scale of referencing. Given the scale of the rates of large-scale vertical motion, and the scale of the average velocity for most natural forms of subsidence, it's possible that the wide-area PIA are affecting the correlation between PSR, geology type, and average velocity.

4.2 London Case Study

Overall, the correlation between average subsidence velocity and PSR is even lower than for the national-level dataset, with a Spearman ρ of 0.038. Tests for correlation with the bedrock geology also yield no discernible variation in the average velocity, whereas, inline with previous studies [20], distinct areas of subsidence were visible in alluvium and beach and tidal flat deposits. Greater levels of subsidence are expected in these deposits as they are susceptible to consolidation and compression; indeed, these areas are some of the few where the average velocity closely aligns with the PSR. As the SubCoast PSRs utilised InSAR data from several European cities either on the coast or situated on river estuaries, it is unsurprising that the PSR values are more aligned with the alluvium subsidence velocities than for other inland areas that have been classified

as clay in the geology supergroup. The majority of these areas are still within the PSR value, and most areas that are subsiding faster than PSR are in close proximity to the Thames, and are located in busy industrial areas including landfill sites, warehouses, and shipping ports to the south of Tilbury and in the north east (see Figure 4.2). For these areas it is likely that the regions of increased subsidence are due to the relatively rapid changing of the landscape from the work that is being conducted (such as the changing number of stored shipping containers), ongoing maintenance, and further compaction from events such as the addition of more landfill waste and the receipt of more shipping goods and containers.

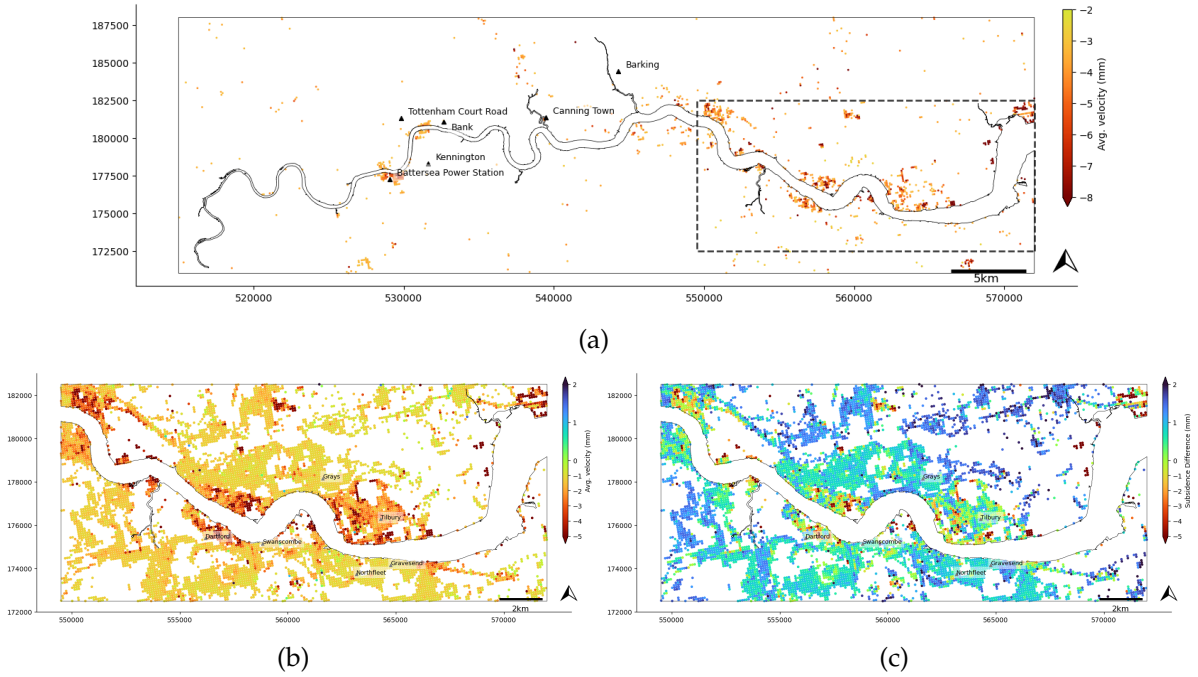

Figure 4.2: Caption

Other areas show clear indications of other processes at work, where the subsidence exceeds PSR but the pattern of deformation differences isn't as speckled as in Figure 4.2c. As presented in the results, one such area is around the Northern Line extension from Kennington to Battersea Power Station. The dominant sources of motion in this area stem from the underground construction work, linking together the stations by creating new sections of tunneling, as well as from groundwater extraction. These results have been replicated elsewhere, with strong correlation found between both the ground deformation velocities and dates of construction activities, as well as the groundwater depletion [17]. Large areas of subsidence are also visible around Tooting, which has also been linked to groundwater abstraction [17].

Broadly, areas north of the Thames estuary experienced more uplift than to the south. This is particularly noticeable around Canning Town and Barking (Figure 4.3). The average velocity over the time period in this area is -1.02 mma^{-1} with a standard deviation of 0.65 mma^{-1}. Although the area is subsiding overall, there are clear areas of uplift throughout 2016 to 2021. In 2016 a large area over Canning Town is uplifting, which subsequently subsides from 2018 to 2021. Conversely, the area around Barking begins to uplift from 2018 through to 2020, before subsiding in 2021. The area around Canning Town was previously identified as an anomalous area due to the slow rates

of subsidence in comparison to the surrounding alluvium, thought to be due to the made ground and alluvium reaching its compaction limit [20]. However, the pattern of subsidence and uplift in the EGMS data is similar to the groundwater extraction and rebound patterns found around the Northern Line extension sites, which could suggest that these effects are related to the groundwater level.

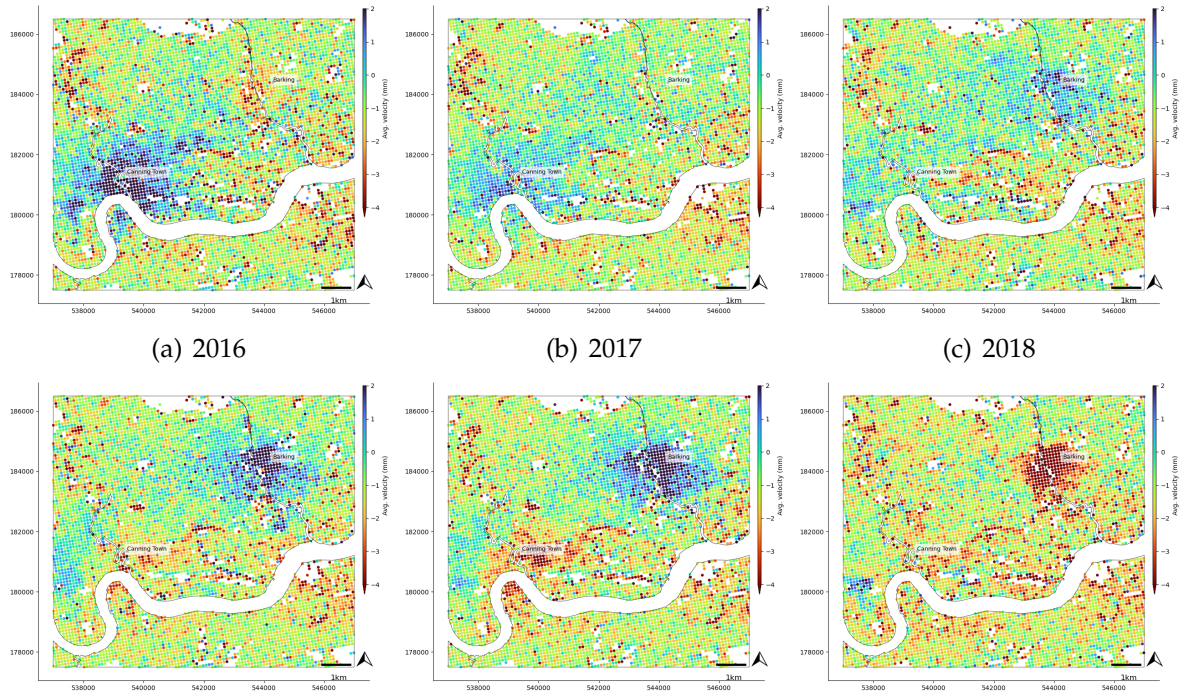

(a) 2016 (b) 2017 (c) 2018

(d) 2019 (e) 2020 (f) 2021

Figure 4.3: Ground motion maps around Barking and Canning Town for 2016 to 2021.

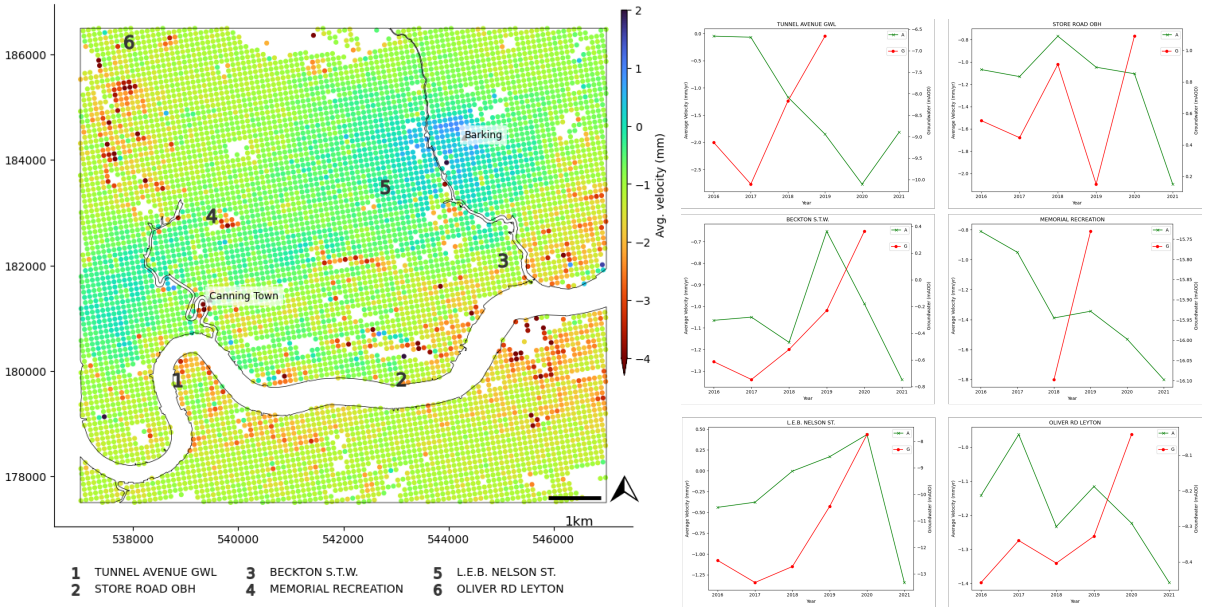

(a) (b)

Figure 4.4: The average velocity for 2016 to 2021 and the locations of boreholes (a), and the yearly average velocities (in green) against groundwater levels for each borehole (in red).

There are 6 boreholes in the surrounding area, depicted in Figure 4.4a. The average

velocity for each borehole was measured using a simple 500 m buffer to average the intersecting EGMS MPs. The yearly average velocity and groundwater levels are included in Figure 4.4b. As can be seen, not all boreholes have measurements for all years; borehole 4 (Memorial Recreation) only has measurements in 2018 and 2019, whereas borehole 1 (Tunnel Avenue GWL) only has measurements between 2016 to 2019. The closest borehole to Canning Town is Memorial Recreation, which only has 2 measurements so no conclusions can be drawn from this. The closest borehole to the Barking area is number 5, L.E.B. Nelson St. The average yearly velocity and groundwater level are correlated, with the groundwater level increasing from -12.49 mAOD in 2016 to -7.74 mAOD in 2020, and the average velocity increasing from -0.44 to 0.44 mma^{-1} from 2016 to 2020, before dropping to -1.34 mma^{-1} in 2021. As there are no measurements for the borehole in 2021 there isn't enough data to confidently attribute the main source of the drop in ground elevation to the groundwater level.

Chapter 5

Conclusion

The initial main aims of this dissertation project were to utilise the downstream InSAR data products from the European Ground Motion Survey (EGMS) to run a national-level analysis into the subsidence rates stemming from the natural geological processes of compaction, dissolution, and shrinkage. This was facilitated by the integration of Potential Subsidence Rates (PSR) and geological information from the SubCoast dataset from the British Geological Survey (BGS), to measure the correlation between the EGMS average velocities and the SubCoast PSRs to 1) understand the relationship between average velocity and the underlying geology type and 2) re-calibrate the PSRs with the new data provided by the EGMS to create an updated PSR map of Britain. Additionally, several ancillary datasets were incorporated to try and separate the sources of motion that were as a result of anthropogenic activity from those that were developing from principally natural processes.

Overall, on a national-level there was negligible correlation between EGMS average velocity metrics and SubCoast PSRs or the underlying geology. For deposits with a potential volume decrease (PSP) of 19% or greater, there was a linear trend with the average velocity and PSP %, and the derived velocity statistic $Wtd\ \mu - 2\sigma$ was similar to PSR. However, for PSPs < 19% there was no correlation between PSR and average velocity. PSRs were then recalibrated using the derived subsidence statistic for PSPs >= 5%, which yielded results with an average difference of 0.40 mma^{-1} compared to the original PSR values, although the linear regression model wasn't representative of the data inputs (negative R^2) and therefore the outputted PSRs have little statistical bearing.

Although there are some areas of fast-moving subsidence, the project showed that, on a national scale, the overwhelming dominant feature of stable subsidence is a large-scale trend of deformation from south to north, with subsidence in large areas of England, Wales, and the Shetland Islands, and uplift in large parts of Scotland, and the local geology types have a limited impact in relation to this. These results appear to corroborate other findings from literature, which attribute these large-scale vertical ground displacements to Postglacial Isostatic Adjustments (PIA) from the deglaciation of the British–Irish ice sheet. Many studies on this topic utilise numerical methods and data inputs such as historic relative sea-level, ice sheet extents, continuous GNSS measurements, and absolute gravity data [54], and the use of InSAR data has been comparatively under utilised (possibly due to the complex data processing and

low-frequency errors that propagate from orbital and atmospheric errors). With the readily available wide-area InSAR ground velocity data from EGMS, perhaps this could be a source of data input for investigating GIA in future.

On a local scale, a case study in the Greater London area was conducted to test the correlation between average velocity and PSR and to identify localised areas that were subsiding at a similar rate to PSR. Some correlations were observed with superficial geology, particularly alluvium deposits around the Thames estuary, but no clear trends between PSR and average velocity were observed. The dominant trends of deformation in the London area appear to stem from the abstraction of groundwater and construction works. However, considering some lithologies, such as Chalk and Clay, the derived velocity statistic was remarkably close to the PSR value; in these instances PSRs could be useful for determining areas of anthropogenic subsidence, which could be utilised in InSAR interpretation tools for assigning causes of motion.

Although the use of the EGMS data wasn't able to validate the PSRs from SubCoast or correlate the average velocities with the underlying geology with strong conviction, the project identified some of the key drivers of subsidence at a national-scale and at a local level. Furthermore, the integration of the EGMS data with SubCoast highlights the ease of running national-level analyses with access to these wide-area big InSAR data products. An extension to this project would be to utilise the full-time series data, rather than just the average velocities, to investigate the correlations with geology type and see if there are any trends between the full deformation signal.

Bibliography

[1] Aquifers | Thames Basin | British Geological Survey (BGS). https://www2.bgs.ac.uk/groundwater/waterResources/thames/aquifers.html. (accessed 2023-08-21).

[2] Battersea and Nine Elms London. https://nineelmslondon.com/transformation/northern-line-extension/. (accessed 2023-08-21).

[3] BGS GeoSure: Compressible ground.

[4] BGS Lexicon of Named Rock Units - London Clay. https://webapps.bgs.ac.uk/lexicon/lexicon.cfm?pub=LC. (accessed 2023-08-20).

[5] BGS Lexicon of Named Rock Units - Result Details. https://webapps.bgs.ac.uk/lexicon/lexicon.cfm?pub=BGS. (accessed 2023-08-20).

[6] BGS Lexicon of Named Rock Units - Thanet Formation. https://webapps.bgs.ac.uk/lexicon/lexicon.cfm?pub=tab. (accessed 2023-08-20).

[7] Enabling access to geological information in support of GMES | PANGEO Project | Fact Sheet | FP7. https://cordis.europa.eu/project/id/262371. (accessed 2023-08-18).

[8] European Ground Motion Service — Copernicus Land Monitoring Service. https://land.copernicus.eu/pan-european/european-ground-motion-service. (accessed 2023-04-11).

[9] IJGI | Free Full-Text | ADAtools: Automatic Detection and Classification of Active Deformation Areas from PSI Displacement Maps. https://www.mdpi.com/2220-9964/9/10/584. (accessed 2023-08-08).

[10] Land Subsidence | U.S. Geological Survey. https://www.usgs.gov/special-topics/water-science-school/science/land-subsidence. (accessed 2023-04-06).

[11] Longest metro lines in European cities 2022. https://www.statista.com/statistics/1129533/longest-metro-lines-in-europe/. (accessed 2023-08-21).

[12] Sizewell C: A New Nuclear Power Station for Britain. https://www.sizewellc.com/. (accessed 2023-08-19).

[13] Spirit Leveling | U.S. Geological Survey. https://www.usgs.gov/centers/land-subsidence-in-california/science/spirit-leveling. (accessed 2023-08-25).

[14] Tunnelling - Crossrail. https://web.archive.org/web/20221228162649/https://www.crossrail (accessed 2023-08-21).

[15] UK natural capital - Office for National Statistics. https://www.ons.gov.uk/economy/environmentalaccounts/bulletins/uknaturalcapitalforpea (accessed 2023-08-15).

[16] What causes sinkholes and where do they occur in the UK?

[17] AGARWAL, V., KUMAR, A., GEE, D., GREBBY, S., GOMES, R. L., AND MARSH, S. Comparative Study of Groundwater-Induced Subsidence for London and Delhi Using PSInSAR. *Remote Sensing 13*, 23 (Jan. 2021), 4741.

[18] AGARWAL, V., KUMAR, A., L. GOMES, R., AND MARSH, S. Monitoring of Ground Movement and Groundwater Changes in London Using InSAR and GRACE. *Applied Sciences 10*, 23 (Jan. 2020), 8599.

[19] AGENCY, U. E. Management of the London Basin Chalk Aquifer - Status Report, Aug. 2018.

[20] ALDISS, D., BURKE, H., CHACKSFIELD, B., BINGLEY, R., TEFERLE, N., WILLIAMS, S., BLACKMAN, D., BURREN, R., AND PRESS, N. Geological interpretation of current subsidence and uplift in the London area, UK, as shown by high precision satellite-based surveying. *Proceedings of the Geologists' Association 125*, 1 (Jan. 2014), 1–13.

[21] BAGHERI-GAVKOSH, M., HOSSEINI, S. M., ATAIE-ASHTIANI, B., SOHANI, Y., EBRAHIMIAN, H., MOROVAT, F., AND ASHRAFI, S. Land subsidence: A global challenge. *Science of The Total Environment 778* (July 2021), 146193.

[22] BANKS, V. Swelling and shrinking soils. https://www.bgs.ac.uk/geology-projects/shallow-geohazards/clay-shrink-swell/. (accessed 2023-04-06).

[23] BATESON, L., CIGNA, F., BOON, D., AND SOWTER, A. The application of the Intermittent SBAS (ISBAS) InSAR method to the South Wales Coalfield, UK. *International Journal of Applied Earth Observation and Geoinformation 34* (Feb. 2015), 249–257.

[24] BATESON, L., EVANS, H., AND JORDAN, C. GMES-service for assessing and monitoring subsidence hazards in coastal lowland areas around Europe. SubCoast D3.5.1. https://nora.nerc.ac.uk/id/eprint/16251/, 2011. (accessed 2023-04-07).

[25] BATESON, L. B., BARKWITH, A. K. A. P., HUGHES, A. G., AND ALDISS, D. T. Terrafirma : London H-3 Modelled Product : Comparison of PS data with the results of a groundwater abstraction related subsidence model. http://www.bgs.ac.uk, 2009. (accessed 2023-07-27).

[26] BGS PRESS, B. G. S. Maps show the real threat of climate-related subsidence to British homes and properties, May 2021.

[27] BRADLEY, S. L., MILNE, G. A., TEFERLE, F. N., BINGLEY, R. M., AND ORLIAC, E. J. Glacial isostatic adjustment of the British Isles: New constraints from GPS measurements of crustal motion. *Geophysical Journal International 178*, 1 (July 2009), 14–22.

[28] CAPES, R., AND PASSERA, E. EGMS Product Description and Format Specification, Feb. 2022.

[29] COSTANTINI, M., MINATI, F., TRILLO, F., FERRETTI, A., NOVALI, F., PASSERA, E., DEHLS, J., LARSEN, Y., MARINKOVIC, P., EINEDER, M., BRCIC, R., SIEGMUND, R., KOTZERKE, P., PROBECK, M., KENYERES, A., PROIETTI, S., SOLARI, L., AND ANDERSEN, H. S. European Ground Motion Service (EGMS). In *2021 IEEE International Geoscience and Remote Sensing Symposium IGARSS* (July 2021), pp. 3293–3296.

[30] CROSETTO, M., SOLARI, L., MRÓZ, M., BALASIS-LEVINSEN, J., CASAGLI, N., FREI, M., OYEN, A., MOLDESTAD, D. A., BATESON, L., GUERRIERI, L., COMERCI, V., AND ANDERSEN, H. S. The Evolution of Wide-Area DInSAR: From Regional and National Services to the European Ground Motion Service. *Remote Sensing 12*, 12 (Jan. 2020), 2043.

[31] CULSHAW, M., AND COOPER, A. H. Dissolution. In *Encyclopedia of Engineering Geology*, P. T. Bobrowsky and B. Marker, Eds., Encyclopedia of Earth Sciences Series. Springer International Publishing, Cham, 2018, pp. 233–235.

[32] DHIR, R. K., DE BRITO, J., MANGABHAI, R., AND LYE, C. Q. 6 - Use of Copper Slag in Geotechnical Applications. In *Sustainable Construction Materials: Copper Slag*, R. K. Dhir, J. de Brito, R. Mangabhai, and C. Q. Lye, Eds. Woodhead Publishing, Jan. 2017, pp. 211–245.

[33] ERKENS, G., BUCX, T., DAM, R., DE LANGE, G., AND LAMBERT, J. Sinking coastal cities. *Proceedings of IAHS 372* (Nov. 2015), 189–198.

[34] FERRETTI, A., MONTI-GUARNIERI, A., PRATI, C., AND ROCCA, F. *InSAR Principles: Guidelines for SAR Interferometry Processing and Interpretation*. ESA Publications, 2007.

[35] FERRETTI, A., PASSERA, E., CAPES, R., SOLARI, L., AND PROIETTI, S. EGMS Algorithm Theoretical Basis Document, Feb. 2023.

[36] FESTA, D., AND DEL SOLDATO, M. EGMStream, a Desktop App for EGMS Data Downstream. *Remote Sensing 15*, 10 (Jan. 2023), 2581.

[37] GALLOWAY, D. L., ERKENS, G., KUNIANSKY, E. L., AND ROWLAND, J. C. Preface: Land subsidence processes. *Hydrogeology Journal 24*, 3 (May 2016), 547–550.

[38] GEE, D., BATESON, L., SOWTER, A., GREBBY, S., NOVELLINO, A., CIGNA, F., MARSH, S., BANTON, C., AND WYATT, L. Ground Motion in Areas of Abandoned Mining: Application of the Intermittent SBAS (ISBAS) to the Northumberland and Durham Coalfield, UK. *Geosciences 7*, 3 (Sept. 2017), 85.

[39] GLOPPER, R. J. D., AND RITZEMA, H. P. Land subsidence. In *Drainage Principles and Applications*. 2006, pp. 477–512.

[40] HANSSEN, R. F. *Radar Interferometry: Data Interpretation and Error Analysis*, vol. 2 of *Remote Sensing and Digital Image Processing*. Springer Netherlands, Dordrecht, 2001.

[41] ISHIBASHI, I., AND HAZARIKA, H. *Soil Mechanics Fundamentals*. CRC Press, Dec. 2010.

[42] JONES, L., BATESON, L., AND CIGNA, F. Modelling Potential Rates of Natural Subsidence using Geological and PSI Ground Motion Data: An Experiment in Europe 3 and Great Britain. *Journal of Marine Science and Engineering* (2021).

[43] KALIA, A. C. Landslide activity detection based on Sentinel-1 PSI datasets of the Ground Motion Service Germany—the Trittenheim case study. *Landslides 20*, 1 (Jan. 2023), 209–221.

[44] KOTZERKE, P., SIEGMUND, R., LANGENWALTER, J., ANDERSEN, H., AND ANDERSEN, A. EGMS Product User Manual, May 2022.

[45] MARKER, B. R. Land Subsidence. In *Encyclopedia of Natural Hazards*, P. T. Bobrowsky, Ed., Encyclopedia of Earth Sciences Series. Springer Netherlands, Dordrecht, 2013, pp. 583–590.

[46] MOREIRA, A., PRATS-IRAOLA, P., YOUNIS, M., KRIEGER, G., HAJNSEK, I., AND PAPATHANASSIOU, K. P. A tutorial on synthetic aperture radar. *IEEE Geoscience and Remote Sensing Magazine 1*, 1 (Mar. 2013), 6–43.

[47] SHAHBAZI, S., CROSETTO, M., AND BARRA, A. GROUND DEFORMATION ANALYSIS USING BASIC PRODUCTS OF THE COPERNICUS GROUND MOTION SERVICE. *The International Archives of the Photogrammetry, Remote Sensing and Spatial Information Sciences XLIII-B3-2022* (May 2022), 349–354.

[48] SOWTER, A., BATESON, L., STRANGE, P., AMBROSE, K., AND SYAFIUDIN, M. F.

DInSAR estimation of land motion using intermittent coherence with application to the South Derbyshire and Leicestershire coalfields. *Remote Sensing Letters 4*, 10 (Oct. 2013), 979–987.

[49] TEAM, T. C. Tube trivia and facts. https://madeby.tfl.gov.uk/2019/07/29/tube-trivia-and-facts/, July 2019. (accessed 2023-08-21).

[50] TEFERLE, F. N., BINGLEY, R. M., ORLIAC, E. J., WILLIAMS, S. D. P., WOODWORTH, P. L., MCLAUGHLIN, D., BAKER, T. F., SHENNAN, I., MILNE, G. A., BRADLEY, S. L., AND HANSEN, D. N. Crustal motions in Great Britain: Evidence from continuous GPS, absolute gravity and Holocene sea level data. *Geophysical Journal International 178*, 1 (July 2009), 23–46.

[51] US DEPARTMENT OF COMMERCE, N. O. A. A. What is glacial isostatic adjustment? https://oceanservice.noaa.gov/facts/glacial-adjustment.html. (accessed 2023-08-24).

[52] VAN ZYL, J., AND KIM, Y. Synthetic Aperture Radar (SAR) Imaging Basics. In *Synthetic Aperture Radar Polarimetry*. John Wiley & Sons, Ltd, 2011, ch. 1, pp. 1–22.

[53] WALTHAM. *Ground Subsidence / by A.C. Waltham.* Blackie, 1989.

[54] WHITEHOUSE, P. L. Glacial isostatic adjustment modelling: Historical perspectives, recent advances, and future directions. *Earth Surface Dynamics 6*, 2 (May 2018), 401–429.

[55] WHITTAKER, B., AND REDDISH, D. Natural Subsidence and Influence of Geological Processes. In *Developments in Geotechnical Engineering*, vol. 56. Elsevier, 1989, pp. 1–13.

[56] WOODHOUSE, I. H. *Introduction to Microwave Remote Sensing*. CRC Press, Boca Raton, Jan. 2017.

[57] ZEITOUN, D. G., AND WAKSHAL, E. The Subsidence Phenomenon Throughout the World. In *Land Subsidence Analysis in Urban Areas: The Bangkok Metropolitan Area Case Study*, D. G. Zeitoun and E. Wakshal, Eds., Springer Environmental Science and Engineering. Springer Netherlands, Dordrecht, 2013, pp. 9–23.

Appendix A

Appendix 1

A.1 EGMS Ortho Data Specification

Parameter	Unit	Description	Data Format
pid	-	MP unique identifier – 10 characters.	Alphanumeric Base 62
easting	m	ETRS89-LAEA.	integer
northing	m	ETRS89-LAEA.	integer
height	m	MP orthometric (geoid) height.	1 DP
rmse	mm	Evaluated on the time series residuals after applying a regression model of a third order polynomial plus a seasonal (sinusoidal) component.	1 DP
mean_velocity	mm/year	Evaluated on the time series residuals after applying a regression model of a first order polynomial plus a seasonal (sinusoidal) component. The value of the field is the first order coefficient of the polynomial.	1 DP
mean_velocity_std	mm/year	Estimated standard deviation of the mean velocity using variance propagation on the regression model, without considering the atmospheric phase screen.	1 DP
acceleration	mm/year2	Evaluated on the time series residuals after applying a regression model of a second order polynomial plus a seasonal (sinusoidal) component. The value of the field is double of the second order coefficient of the polynomial (considering a model of the kind $\alpha_0 + \alpha_1 x + \alpha_2^2 x^2$).	2 DP
acceleration_std	mm/year2	Estimated standard deviation of the acceleration using variance propagation on the regression model.	2 DP

Table A.1: A description of the data columns provided in the EGMS Ortho data product. Source: EGMS Product Description and Format Specification.

A.2 Mining Hazards

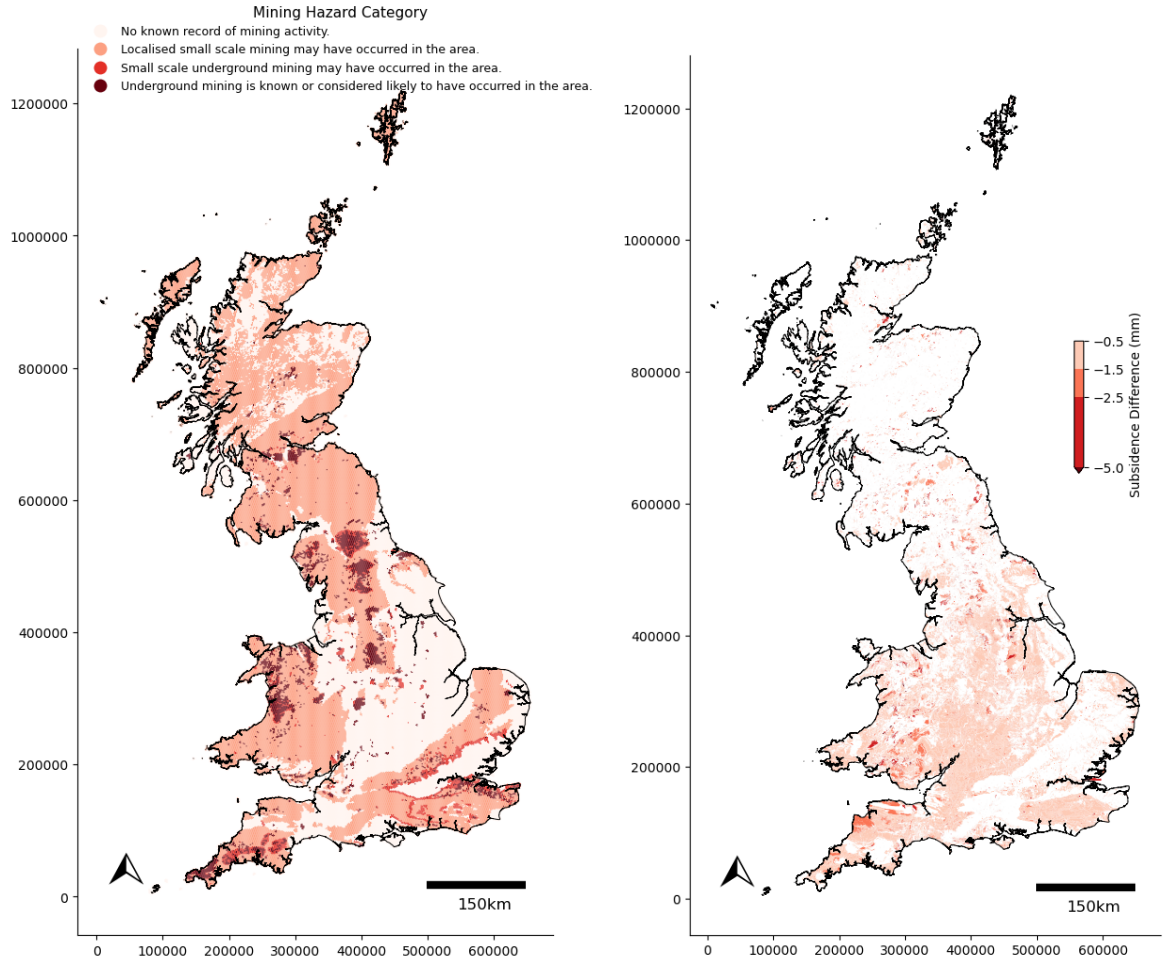

(a) Mining Hazards (b) Avg. Subsidence Velocity

Figure A.1: Maps showing potential mining hazard areas and subsidence velocity. Subsiding areas are included where the average velocity < 0.5 mma^{-1} and the overall PSP is < 0.

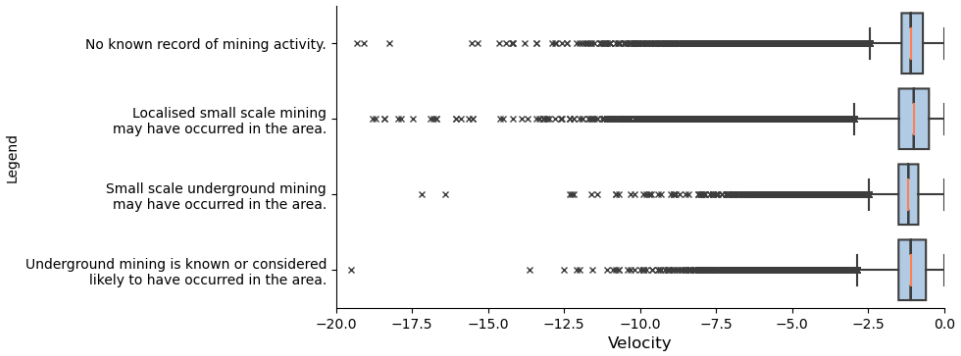

Figure A.2: Distribution of subsidence velocity by mining hazard category. Average velocities are slightly lower for the small scale and underground mining, however these aren't significantly different.